



# Improved gas metal arc welding multi-physics process model and its application to MIL A46100 armor-grade steel butt-welds

M. Grujicic, J.S. Snipes, R. Galgalikar, S. Ramaswami and R. Yavari  
*Department of Mechanical Engineering, Clemson University, Clemson, South Carolina, USA, and*  
 C.-F. Yen, B.A. Cheeseman and J.S. Montgomery  
*Army Research Laboratory, Survivability Materials Branch, Aberdeen Proving Ground, Aberdeen, Maryland, USA*

## Abstract

**Purpose** – The purpose of this paper is to develop multi-physics computational model for the conventional gas metal arc welding (GMAW) joining process has been improved with respect to its predictive capabilities regarding the spatial distribution of the mechanical properties (strength, in particular) within the weld.

**Design/methodology/approach** – The improved GMAW process model is next applied to the case of butt-welding of MIL A46100 (a prototypical high-hardness armor-grade martensitic steel) workpieces using filler-metal electrodes made of the same material. A critical assessment is conducted of the basic foundation of the model, including its five modules, each dedicated to handling a specific aspect of the GMAW process, i.e.: first, electro-dynamics of the welding-gun; second, radiation/convection controlled heat transfer from the electric arc to the workpiece and mass transfer from the filler-metal consumable electrode to the weld; third, prediction of the temporal evolution and the spatial distribution of thermal and mechanical fields within the weld region during the GMAW joining process; fourth, the resulting temporal evolution and spatial distribution of the material microstructure throughout the weld region; and fifth, spatial distribution of the as-welded material mechanical properties.

**Findings** – The predictions of the improved GMAW process model pertaining to the spatial distribution of the material microstructure and properties within the MIL A46100 butt-weld are found to be consistent with general expectations and prior observations.

**Originality/value** – To explain microstructure/property relationships within different portions of the weld, advanced physical-metallurgy concepts and principles are identified, and their governing equations parameterized and applied within a post-processing data-reduction procedure.

**Keywords** Gas metal arc welding (GMAW), MIL A46100 armor-grade steel, Multi-Physics Process Modelling

**Paper type** Research paper

## 1. Introduction

The gas metal arc welding (GMAW) process falls into the class of consumable electrode arc welding processes. To help with the explanation of the basics of the GMAW process, a simple schematic is provided in Figure 1. It should be noted that the labeled schematic shown in Figure 1 pertains to the case of the conventional gas metal arc butt (side-to-side) welding process. A summary of the essential features, process parameters, main advantages and limitations of the GMAW can be found in our prior work (Grujicic *et al.*, 2013a, b, c).

The present work deals with GMAW of armor-grade martensitic steels. In our prior work (Grujicic *et al.*, 2013a, b, c), a detailed presentation was given of: first, the thermal



Report Documentation Page		Form Approved OMB No. 0704-0188
Public reporting burden for the collection of information is estimated to average 1 hour per response, including the time for reviewing instructions, searching existing data sources, gathering and maintaining the data needed, and completing and reviewing the collection of information. Send comments regarding this burden estimate or any other aspect of this collection of information, including suggestions for reducing this burden, to Washington Headquarters Services, Directorate for Information Operations and Reports, 1215 Jefferson Davis Highway, Suite 1204, Arlington VA 22202-4302. Respondents should be aware that notwithstanding any other provision of law, no person shall be subject to a penalty for failing to comply with a collection of information if it does not display a currently valid OMB control number.		
1. REPORT DATE <b>2014</b>	2. REPORT TYPE	3. DATES COVERED <b>00-00-2014 to 00-00-2014</b>
4. TITLE AND SUBTITLE <b>Improved Gas Metal Arc Welding Multi-physics Process Model and its Application to MIL A46100 Armor-grade Steel Butt-welds</b>		5a. CONTRACT NUMBER
		5b. GRANT NUMBER
		5c. PROGRAM ELEMENT NUMBER
6. AUTHOR(S)	5d. PROJECT NUMBER	
	5e. TASK NUMBER	
	5f. WORK UNIT NUMBER	
7. PERFORMING ORGANIZATION NAME(S) AND ADDRESS(ES) <b>Clemson University, Department of Mechanical Engineering, 241 Engineering Innovation Building, Clemson, SC, 29634</b>		8. PERFORMING ORGANIZATION REPORT NUMBER
9. SPONSORING/MONITORING AGENCY NAME(S) AND ADDRESS(ES)		10. SPONSOR/MONITOR'S ACRONYM(S)
		11. SPONSOR/MONITOR'S REPORT NUMBER(S)
12. DISTRIBUTION/AVAILABILITY STATEMENT <b>Approved for public release; distribution unlimited</b>		
13. SUPPLEMENTARY NOTES		
14. ABSTRACT <b>Purpose ??? The purpose of this paper is to develop multi-physics computational model for the conventional gas metal arc welding (GMAW) joining process has been improved with respect to its predictive capabilities regarding the spatial distribution of the mechanical properties (strength in particular) within the weld. Design/methodology/approach ??? The improved GMAW process model is next applied to the case of butt-welding of MIL A46100 (a prototypical high-hardness armor-grade martensitic steel) workpieces using filler-metal electrodes made of the same material. A critical assessment is conducted of the basic foundation of the model, including its five modules, each dedicated to handling a specific aspect of the GMAW process, i.e.: first, electro-dynamics of the welding-gun; second, radiation/convection controlled heat transfer from the electric arc to the workpiece and mass transfer from the filler-metal consumable electrode to the weld; third, prediction of the temporal evolution and the spatial distribution of thermal and mechanical fields within the weld region during the GMAW joining process; fourth, the resulting temporal evolution and spatial distribution of the material microstructure throughout the weld region and fifth, spatial distribution of the as-welded material mechanical properties. Findings ??? The predictions of the improved GMAW process model pertaining to the spatial distribution of the material microstructure and properties within the MIL A46100 butt-weld are found to be consistent with general expectations and prior observations. Originality/value ??? To explain microstructure/property relationships within different portions of the weld, advanced physical-metallurgy concepts and principles are identified, and their governing equations parameterized and applied within a post-processing data-reduction procedure.</b>		
15. SUBJECT TERMS		

16. SECURITY CLASSIFICATION OF:			17. LIMITATION OF ABSTRACT <b>Same as Report (SAR)</b>	18. NUMBER OF PAGES <b>35</b>	19a. NAME OF RESPONSIBLE PERSON
a. REPORT <b>unclassified</b>	b. ABSTRACT <b>unclassified</b>	c. THIS PAGE <b>unclassified</b>			

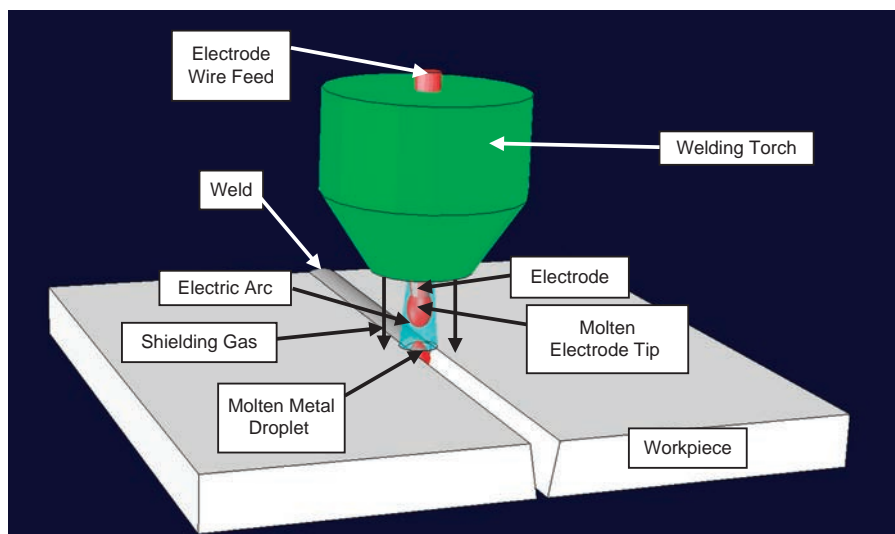


**Figure 1.**  
A schematic  
representation of the  
conventional gas metal arc  
welding (GMAW) process

histories of the fusion zone (FZ) and heat-affected zone (HAZ); and second, welding-induced changes in the weld microstructure of this class of steels during GMAW. Hence, these details will not be repeated here.

A detailed overview of the past GMAW-process modeling efforts, their strengths and limitations, as well as a preliminary classification of these models, was presented in our prior work (Grujicic *et al.*, 2013c). The key observation of this overview was that the present GMAW process models tend to address in sufficient detail only specific aspects of this process and grossly oversimplify or neglect the other aspects. To overcome this limitation, a preliminary multi-physics GMAW process model was introduced in our recent work (Grujicic *et al.*, 2013c). However, this GMAW process model was not fully developed relative to its capability to predict the spatial distribution of the mechanical properties within the weld. Hence, the main objective of the present work is to improve the multi-physics GMAW process model, which is capable of relating the GMAW process parameters, workpiece-material chemical composition and microstructure, and weld geometry to the temporal evolution and the spatial distribution of material microstructure and properties within the FZ and HAZ. The specific improvements pertain to the capability of this process model to predict the distribution of the mechanical properties within the weld from the knowledge of the corresponding distribution of the weld microstructure. These improvements are both of a general character and of a specific character (i.e. they are finely tuned for predicting weld-property distribution within MIL A46100).

## 2. Multi-physics GMAW process model

In this section, a concise overview is provided of our recently developed multi-physics GMAW process model (Grujicic *et al.*, 2013c). As mentioned earlier, the model is comprised of a series of five modules, each of which handles a different aspect of the GMAW process and communicates/exchanges information with the neighboring module(s). To help clarify the process-model structure, a flowchart revealing the sequence and interconnectivity of the modules is depicted in Figure 2. In the remainder

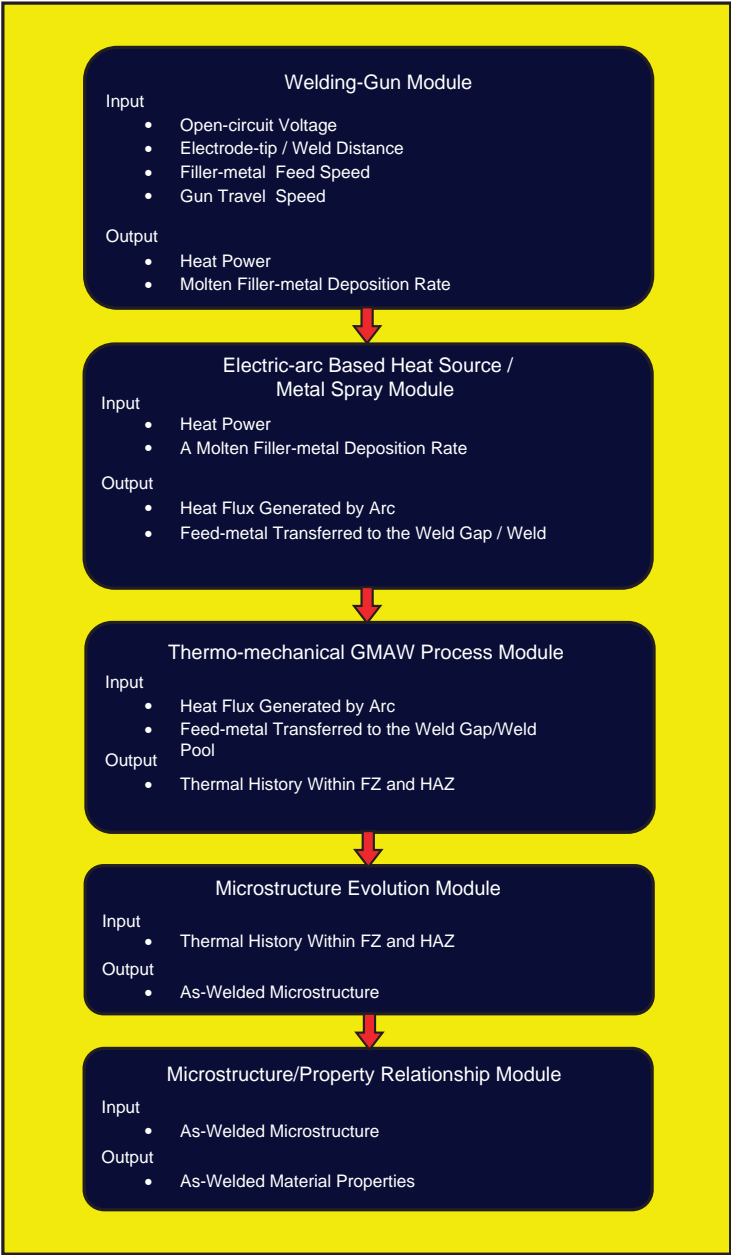


**Figure 2.**  
The structure of the multi-physics GMAW process model consisting of five modules as proposed by Grujicic *et al.* (2013c)

of this section, a brief description is provided of the key governing functional relationships, as well as of the procedures used for calibration and validation of modules. Additional details could be found in Grujicic *et al.* (2013c).

### 2.1 Welding-gun module

The main purpose of this module is to establish functional relationships between the welding gun input parameters: open-circuit voltage; welding current; electrode diameter; electrode-tip/weld distance; filler-metal feed speed; and gun-travel speed, and the welding gun output parameters, primarily the output heat power/power density and the filler-metal transfer rate from the tip of the consumable electrode to the weld pool. These functional relationships are parameterized/calibrated using an experimental approach. Within this approach, a parametric study over the aforementioned welding-gun input parameters is carried out while the output parameters voltage, current, power and deposition/spray rate are directly measured. The governing relations are then parameterized using these experimental results through the application of either a multiple regression or a neural network-type procedure.

In the present work, no attempt was made to improve the capabilities of this module beyond their counterparts found in the original process module (Grujicic *et al.*, 2013c).

Typical results yielded by the present module are depicted in Figure 3(a)-(b), in which temporal evolutions of the welding voltage (input) and the welding power (output) are shown, respectively. It is seen that, even when the input voltage is set to a constant value, the resulting output power shows considerable fluctuations. Consequently, it is the functional relationship between the input voltage and mean output power that is established by this module and passed to the next module.

### 2.2 Electric-arc-based heat-source/metal spray module

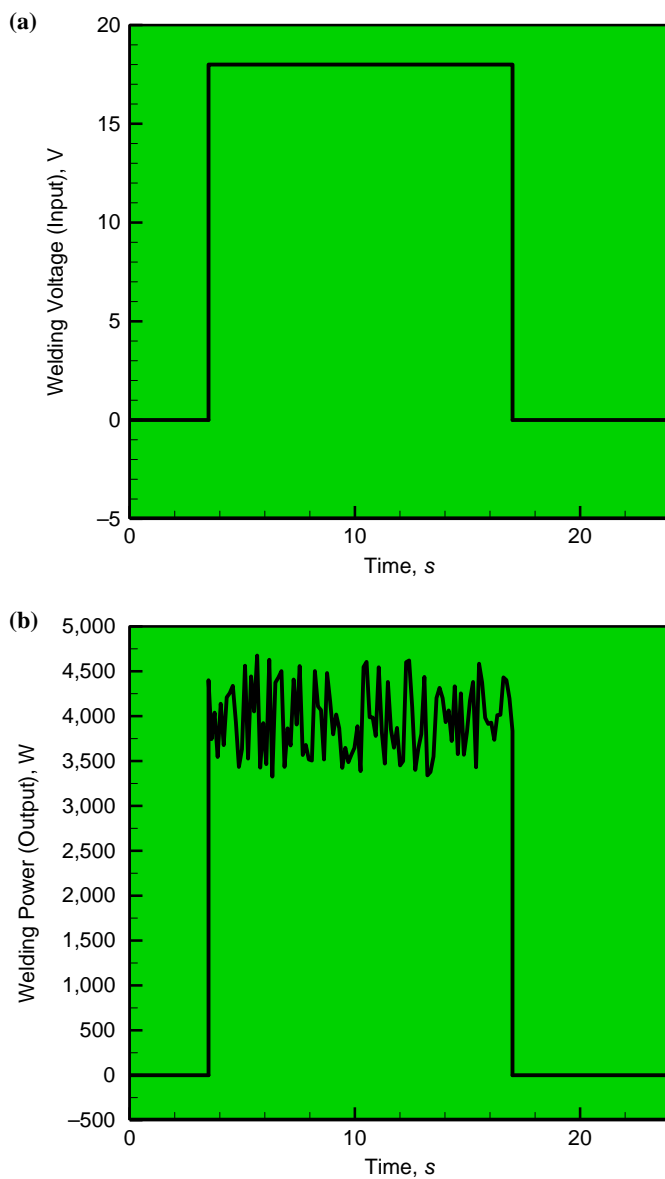
The main purpose of this module is to utilize the outputs of the welding-gun module (specifically, the output (heat) power and the filler-metal transfer rate from the electrode to the weld pool) and to determine the distributions of: the heat-flux; and the filler-metal transfer rate, both over the weld-pool top surface.

In agreement with a number of experimental studies (e.g. Pavelic *et al.*, 1969), the module assumes that heat flux (as well as filler-metal deposition rate) distributions are of a normal-circular type. The circular-normal distribution function for heat flux  $q(r)$  as a function of the radial distance from the electrode axis,  $r$ , is given as:

$$q(r) = q_0 \exp\left(\frac{-r^2}{r_\sigma^2}\right) \quad (1)$$

where  $q(0)$  is the heat flux peak value while  $r_\sigma$  is a (standard-deviation type) measure of the width of the power-density distribution function.

Examination of the heat flux distribution function, Equation (1), reveals the presence of two model parameters,  $q(0)$  and  $r_\sigma$ . These two parameters are determined using the following procedure: first, it is established that the two parameters are mutually related by the constraint that the surface integral of  $q(r)$  with  $r$  ranging from zero to infinity must be equal to the electrode-based total input heat power, as yielded by the welding-gun module; and second, by using the results of experimental techniques such as infra-red surface thermometry (Kim, 2012), which provide quantitative information regarding the decrease in the surface heat flux with an increase in the radial



**Notes:** (a) The input voltage; and (b) the output power

distance from the electrode axis. More details regarding the Equation (1) parameterization procedure can be found in Grujicic *et al.* (2013c).

The spatial distribution of the filler-metal transfer rate is given by a two-parameter equation analogous to Equation (1). The two model parameters are determined using a procedure similar to that employed using parameterization of Equation (1), specifically: it is recognized that the two parameters are mutually related by the

constraint that the surface integral of the filler-metal transfer rate distribution function for  $r$  ranging between zero and infinity must be equal to the total filler-metal transfer rate (as output by the welding-gun module); and by using the results of experimental techniques, such as experimental characterization of the surface profile of the weld bead, which provide quantitative information regarding the decrease in the filler-metal transfer rate with distance from the weld symmetry plane. More details regarding this model calibration procedure can be found in Grujicic *et al.* (2013c).

In the present work, no attempt was made to improve this module via either reformulation of the governing equations or via improved parameterization of the governing equations used in the original electric-arc-based heat-source/metal spray module (Grujicic *et al.*, 2013c).

A three-dimensional surface plot of  $q(r)/q_0$  as a function of distances along the weld transverse direction ( $x$ ) and the weld longitudinal direction ( $y$ ) is depicted in Figure 4. It should be noted that  $x$ ,  $y$  and  $r_\sigma = 1/3$  are all normalized by the (equal transverse and longitudinal) workpiece half-edge lengths.

### 2.3 Thermo-mechanical GMAW process module

The main purpose of this module is to utilize the heat flux and filler-metal transfer rate distribution results yielded by the electric-arc-based heat source/metal spray module, as boundary conditions, within a transient fully coupled thermo-mechanical

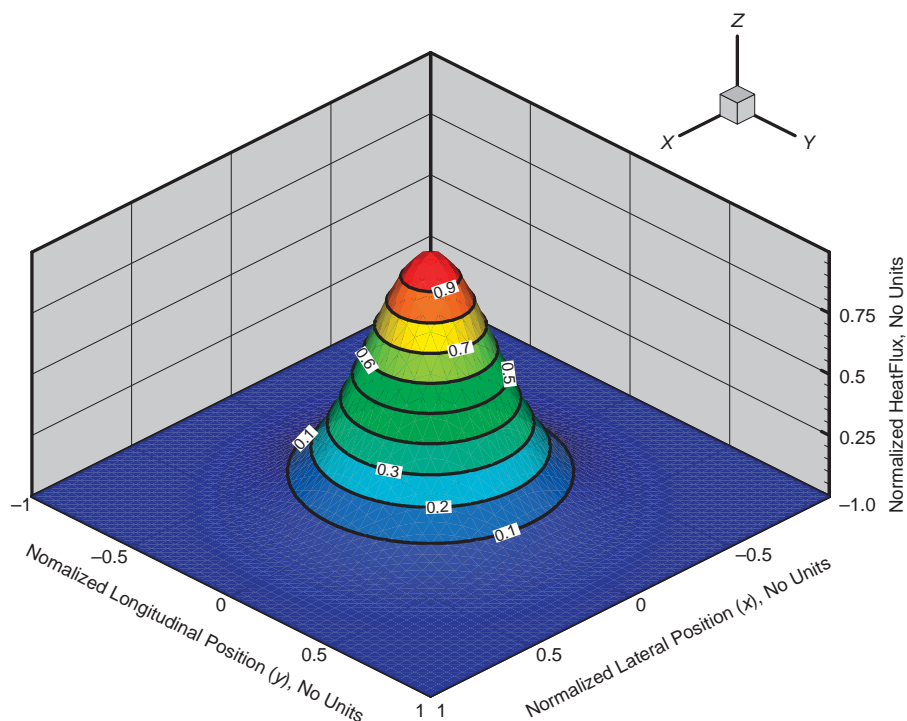


**Figure 4.** A normalized heat-flux three-dimensional surface plot (for the case of the circular-normal distribution) as a function of the lateral and longitudinal locations (normalized by the corresponding workpiece half-edge lengths) on the workpiece top surface

**Notes:** The  $x = y = 0$  location, associated with the maximum heat flux, corresponds to the current position of the electrode axis

finite-element GMAW process analysis to determine the temporal evolution and the spatial distribution of various thermo-mechanical fields. This module is effectively an adaptation of a Friction Stir Welding process model reported recently by Grujicic and co-workers (2010a, b, c, 2011a, b, c, 2012a, b, c, d, 2013d). The transient thermo-mechanical finite-element analysis used within this module typically requires specification of the following aspects of the problem being analyzed: geometrical model; meshed model; computational algorithm; initial conditions; boundary conditions; material model(s); and computational tool.

A schematic of the prototypical geometrical model used in the thermo-mechanical GMAW process module is depicted in Figure 5(a). It is seen that the geometrical model comprises two workpieces to be butt-welded, which initially (i.e. before welding) possess a rectangular-paralleliped shape with the prototypical dimensions,  $L_x = 60$  mm,  $L_y = 60$  mm and  $L_z = 10$  mm. As indicated in Figure 5(b), the edges of the

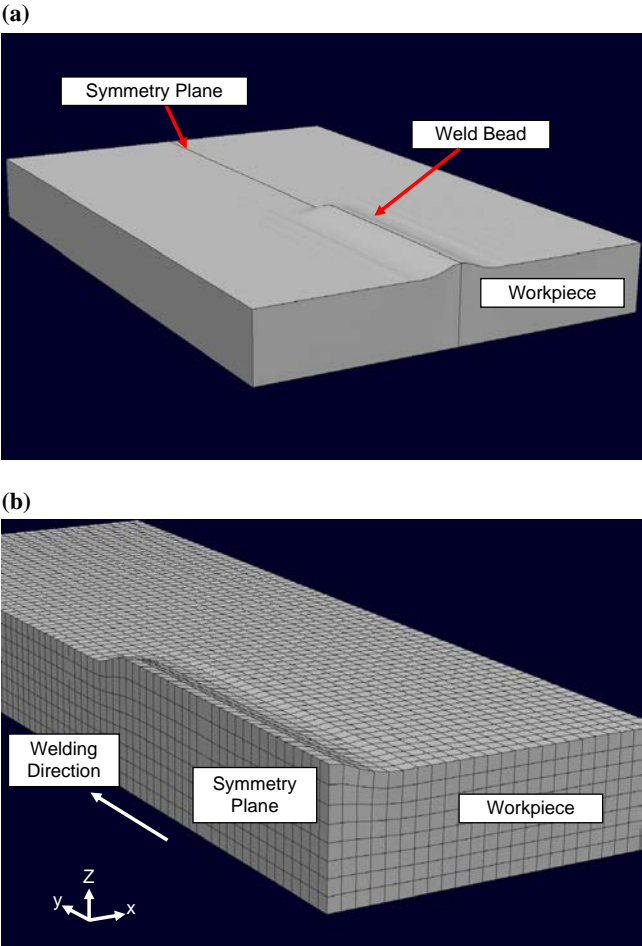


**Figure 5.**  
Typical models used in the  
thermo-mechanical  
GMAW process module

**Notes:** (a) Geometrical (after reflection across the weld boundary); and (b) meshed (not reflected)

parallelepiped are aligned with the global  $x$ - $y$ - $z$  Cartesian coordinate system. Also, as seen in Figure 5(a)-(b), the geometrical model is oriented in such a way that: the weld symmetry plane is orthogonal to the  $x$ -axis; the weld gun travels along the  $y$ -direction; while the workpiece through-the-thickness upward normal direction is aligned with the  $z$ -axis. The origin of the coordinate system ( $x = y = z = 0$ ) is placed at the mid-value of  $x$ , minimum value of  $y$  and at the minimum value of  $z$  of the computational domain (geometrical model).

When a GMAW process is modeled in the open literature, different approaches are used to define the size and the shape of the weld pool/FZ. In some of these approaches, the size and the shape of the weld pool/FZ is predetermined (e.g. Grujicic *et al.*, 2013a, b). This approach is not totally justified since, in the real GMAW process, the size and shape of the weld pool/FZ is controlled by dynamic interactions between the electric arc, a stream of filler-metal droplets being transferred from the melted electrode, and the workpiece. That is the reason that in the thermo-mechanical GMAW process module, the size and shape of the weld pool/FZ were not predefined (as an input to the analysis), but rather were determined from the results yielded by the analysis. Specifically, the boundary between the HAZ and the weld pool/FZ is set to coincide with the computed liquidus-temperature iso-surface. As far as the top surface of the weld pool/FZ, and the formation of the weld bead, are concerned they are dynamically reshaped, during the analysis, in accordance with the advancement of the weld gun and the aforementioned filler-metal transfer-rate circular-normal distribution function (as defined in the electric-arc-based heat-source/metal-spray module). An example of the resulting geometry of the two workpieces to be butt-welded, at an instant when the weld gun has traveled approximately one-third of the distance in the  $y$ -direction, is depicted in Figure 5(a).

It should be noted that when the geometrical model of the type shown in Figure 5(a) is used, the computational domain is symmetric about  $x = 0$  and, hence, only one half of this computational domain has to be explicitly analyzed. Typically, the results presented in the remainder of the manuscript will refer to the right (when looking along the direction of motion of the welding gun) half of the computational domain.

The selected half of the computational domain is meshed using eight-node, first-order, thermo-mechanically coupled, reduced-integration, hexahedral continuum elements. An example of the (close-up of the) typical meshed model used in the present work is displayed in Figure 5(b). The model shown in Figure 5(b) contains 13,824 elements. Meshed models containing between 1,728 and 110,592 elements were also investigated in the present work. The meshed model displayed in Figure 5(b) is found to be the best compromise between computational accuracy and computational cost. Examination of Figure 5(b) clearly reveals the presence of the deposited weld bead over the top portion of the workpiece surface traversed by the weld gun.

Within the thermo-mechanical GMAW process module, a transient, fully coupled, thermo-mechanical, unconditionally stable, implicit finite-element algorithm is utilized. Development of the thermo-mechanical fields within the weld during the GMAW process is analyzed in the following way: first, before the analysis is started, the computational domain is supported over its bottom ( $z = 0$ ) face, made stress-free and placed at the ambient temperature; second, after the GMAW process is initiated, the electric-arc heat flux and the filler-metal transfer, represented by their respective circular-normal distribution functions are applied to the top surface of the weldment and advanced in the welding (positive  $y$ ) direction to follow the traversal of the weld gun; third, to account for additional thermal effects associated with the transfer of the

filler-metal from the melted electrode tip to the weld pool, a (volumetric) heat source described by a relation analogous to Equation (1) is introduced into the top layer of the workpiece elements. In addition, the (volumetric) heat source is tied to the weld gun and forced to track the gun's position during welding; fourth, electromagnetic stirring of the weld pool is not modeled explicitly. Rather, its effect is accounted for by setting the thermal conductivity of the workpiece material to a higher value when the temperature of the workpiece material exceeds the liquidus temperature (i.e. within the weld pool); fifth, thermal convection and radiation are activated in order to account for thermal interactions between the weldment and the environment. Concurrently, heat transfer within the weldment, including the FZ, is assumed to take place via conduction; sixth, due to the thermo-mechanical character of the analysis and the non-uniformities in thermal fields within the weldment, thermal stresses are generated during the welding process. In addition, in the regions in which thermal stresses acquire sufficiently high magnitude, local permanent deformations/distortions and residual stresses are allowed to develop; and seventh, in the cases when high thermal stresses caused the development of permanent distortions, following the standard practice, 95 percent of the work of plastic deformation is assumed to be dissipated in the form of heat while the remaining 5 percent is assumed to be stored in the form of local microstructural and crystal defects (primarily dislocations).

At the beginning of the analysis, the workpiece material is assumed to be at room/ambient temperature and stress-free.

During the analysis, the following boundary conditions are applied: mechanical and thermal symmetry boundary conditions, over the  $x=0$  symmetry plane; zero vertical-displacement boundary conditions, over the bottom face of the workpiece/weldment; a radial normally distributed heat flux (advancing in the welding direction) over the top surface of the workpiece; natural convection and radiation boundary conditions over all exposed surfaces of the workpiece/weldment; and zero normal flux thermal boundary conditions over the bottom surface of the workpiece/weldment.

The major simplification used in, and perhaps the greatest weakness of the thermo-mechanical GMAW process module concerns decoupling between the thermo-mechanical and microstructural evolution aspects of the material within the weld. Specifically, the thermo-mechanical GMAW process module enables the generation of thermal histories of the material points and final strain/stress fields within the weld pool/FZ and HAZ, while neglecting the contribution of various phase transformations and microstructure-evolution processes to the thermal and mechanical response of the material within the weld region. In other words, the thermo-mechanical analysis utilizes a single-phase non-transforming workpiece-material model. Subsequently, the resulting thermal histories of the material points within the weld region are used in the fourth module, the microstructure evolution module, in order to determine the role of various phase transformations on the local distribution of the material microstructure within the weld region. In addition, the stress/strain fields yielded by the thermo-mechanical GMAW process module are used in the fifth module, the microstructure/property relationship module. Clearly, this approach neglects the role of the continuously evolving local material microstructure on the material response during the GMAW joining process, and this shortcoming is not the subject of the present work, but will be addressed in our future work.

Within the current rendition of the thermo-mechanical GMAW process model, the workpiece material and the filler-metal (assumed to be chemically identical to the workpiece material) are assumed to be homogeneous, single-phase and capable of

undergoing liquid-to-solid phase transformation, but not any of the solid/solid phase transformations. Since it is assumed that the workpiece and filler-metal electrode are made of the same material, the thermo-mechanical analysis requires the knowledge of a single material model. However, due to the thermo-mechanical character of the finite-element analysis utilized, both thermal and mechanical aspects of the material model have to be defined.

The thermal-portion of the material is defined by prescribing the values and temperature dependencies (where applicable) of the following quantities: material mass density,  $\rho$ , specific heat,  $C_p$ , and thermal conductivity,  $k$ , for the heat-conduction part of the model; the heat transfer coefficient,  $h$ , and the sink temperature,  $T_{\text{sink}} (= T_{\text{room}})$ , for the natural-convection part of the model; and emissivity,  $\varepsilon$ , and the ambient temperature,  $T_{\text{amb}} (= T_{\text{room}})$ , for the radiation part of the model.

As far as the material's mechanical response is concerned, it is assumed to be isotropic (linearly) elastic, and (strain-hardenable, strain-rate sensitive, thermally softenable) plastic. The elastic response of the material is defined using the generalized Hooke's law, in which the elastic strain is represented as a difference between the total and the thermal strains. The thermal strain, in turn, is related to the temperature deviation from a reference value (the room temperature) using the isotropic linear expansion coefficient  $\alpha$ , a scalar, temperature-dependent quantity.

As far as the plastic response of the material is concerned, it is described using the following three relations:

- (1) a yield criterion, i.e. a stress-based scalar relation which defines the condition that must be satisfied for the onset (and continuation) of plastic deformation;
- (2) a flow rule, i.e. a mathematical relation which describes the rate of change of different plastic-strain components in the course of plastic deformation; and
- (3) a constitutive law, i.e. a mathematical relation which describes the changes in material strength as a function of the extent of plastic deformation, the rate of deformation and temperature.

In the current rendition of the thermo-mechanical GMAW process module, the constitutive law is represented using the Johnson-Cook material-model formulation (Johnson and Cook, 1983).

For MIL A46100, the steel grade analyzed in the present work, plastic deformation is considered to be of a purely distortional (volume-preserving) character and, consequently, the yield criterion and the flow rule are, respectively, defined using the von Mises yield criterion and a normality flow rule. According to the von Mises yield criterion, the (von Mises) equivalent stress (a scalar quantity related to the second invariant of the stress deviator) must reach the value of the material yield strength for plastic deformation to commence/continue. The normality flow-rule, on the other hand, states that the plastic flow takes place in the direction of the stress-gradient of the yield surface (a locus of the stress points within the associated multidimensional stress space at which the von Mises stress criterion is satisfied). As far as the Johnson-Cook strength constitutive law used is concerned, it models the material strength as a product of four terms:

- (1) strength of the as-received pre-weld material;
- (2) an irreversible strain-hardening factor;
- (3) a reversible strain-rate hardening factor; and
- (4) a reversible thermal-softening factor.

MMMS  
10,2

186

According to the Johnson-Cook material model, material strength falls to zero at temperatures in excess of the material solidus temperature. However, this loss of strength is reversible, and the material strength reassumes non-zero positive values at temperatures lower than the solidus temperature.

A summary of the room-temperature values for all the MIL A46100 thermal, mechanical and thermo-mechanical model parameters used in the present work is provided in Tables I and II. It should be noted that the values for the material-property parameters listed in these tables are prototypical for the as-received condition of MIL A46100 at room temperature. As mentioned above, these values will change during the GMAW process to account for the local effects of cumulative plastic strain, instantaneous temperature and strain rate. However, the effect of the microstructural changes within the weld during the GMAW process on the values of the material properties is not accounted for in the current rendition of the thermo-mechanical GMAW process module.

The computational analysis implemented in the thermo-mechanical GMAW process module utilizes an implicit solution algorithm built-in ABAQUS/Standard, a general-purpose finite element solver (Dassault Systemes, 2011). In addition, in order to handle the spatially non-uniform and time-varying heat flux, the DFLUX user subroutine is used within the module. This general-purpose boundary-condition subroutine enables specification of the non-uniform distributed flux in combined heat transfer/mass diffusion type of analyses.

While some deficiencies of the present module have been identified earlier in the manuscript, no attempt was made, in the present work, to eliminate these shortcomings.

A few characteristic results yielded by the present module for the case of MIL A46100 GMAW butt-welding are presented in the remainder of this section.

**Table I.**  
Johnson-cook strength  
model material  
parameters  
for MIL A46100

Parameter	Symbol	Units	Value
Young's modulus	$E$	Gpa	205-215
Poisson's ratio	$\nu$	N/A	0.285-0.295
Reference strength	$A$	Mpa	1,000-1,100
Strain-hardening parameter	$B$	MPa	250.0
Strain-hardening exponent	$n$	n/a	0.12
Strain-rate coefficient	$C$	n/a	0.02
Room temperature	$T_{\text{room}}$	K	298.0
Melting temperature	$T_{\text{melt}}$	K	1,720
Temperature exponent	$m$	n/a	0.5

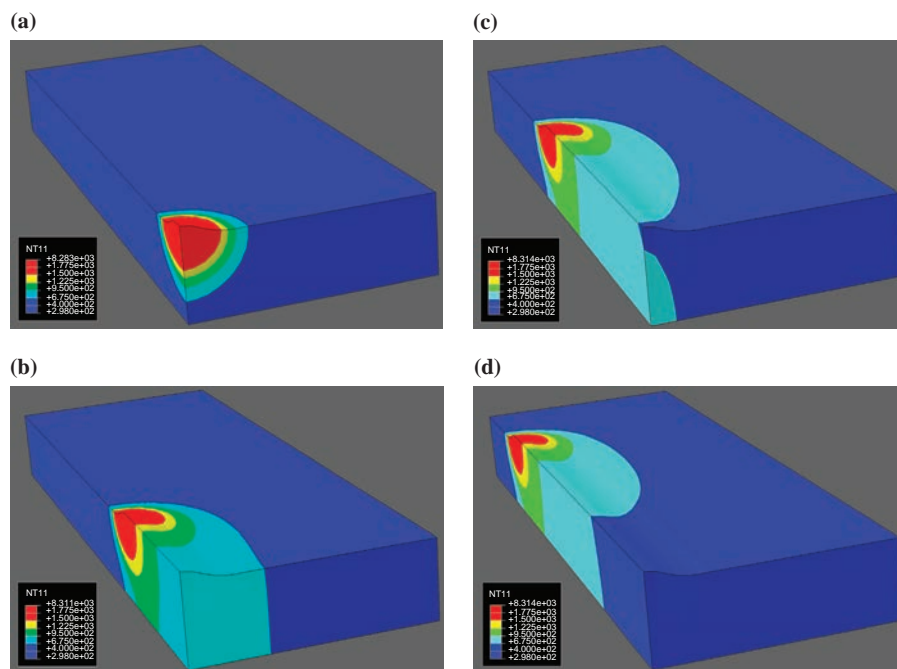
**Table II.**  
General, thermo-  
mechanical and  
thermal parameters  
for MIL A46100

Parameter	Symbol	Units	Value
Material mass density	$\rho$	kg/m <sup>3</sup>	7,840-7,860
Coefficient of linear thermal expansion	$\alpha$	1/K	11e-6-12e-6
Specific heat	$C_p$	J/kg K	440-520
Thermal conductivity	$k$	W/m K	35-50
Heat transfer coefficient	$h$	W/m <sup>2</sup> K	45
Sink temperature	$T_{\text{sink}}$	K	298
Emissivity	$\varepsilon$	n/a	0.57
Ambient temperature	$T_{\text{amb}}$	K	298

Figure 6(a)-(d) show typical results pertaining to the temporal evolution of the temperature field within the weld region over the (analyzed) right-portion of the weldment. The results displayed in Figure 6(a)-(d) are obtained at relative welding times of 0.6, 2.1, 3.6 and 4.8 s, respectively, and for the following selection of the GMAW process parameters: welding input voltage = 30 V, welding current = 200 A, electrode diameter = 1 mm, electrode-tip/weld distance = 1.3 cm, electrode feed-rate = 10 cm/s, and gun travel speed = 1 cm/s. To improve clarity, regions of the weldment with a temperature exceeding the liquidus temperature are denoted using red.

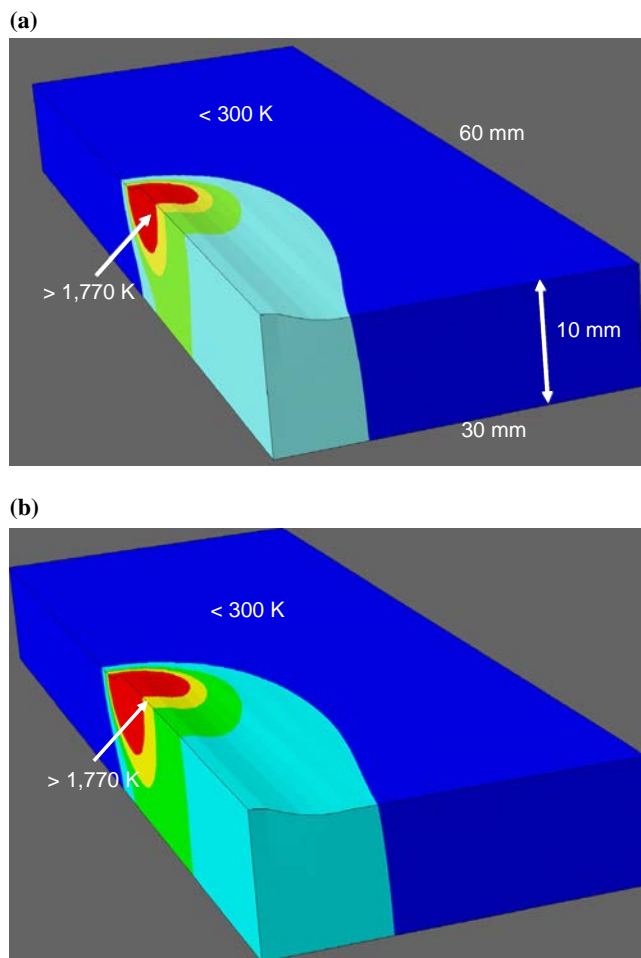
Examination of the results displayed in Figure 6(a)-(d) reveals that: the FZ, after a brief transient period, acquires a nearly constant size and shape, as it moves along the welding direction (to track the position of the weld gun); as welding proceeds, natural convection and radiation to the surroundings, together with conduction through the adjacent workpiece material region, cause the previously molten material within the FZ to solidify (and to continue to cool); and under the given welding conditions, the FZ extends downward by approximately 40-45 percent of the workpiece thickness.

The effect of GMAW process parameters on the temperature distribution is exemplified by the results depicted in Figure 7(a)-(b). The results displayed in these figures were obtained under identical GMAW process conditions except for the value of the input welding voltage, set equal to 30 and 35 V for the cases displayed in Figure 7(a)-(b),



**Notes:** (a) 0.6 s; (b) 2.1 s; (c) 3.6 s; and (d) 4.8 s under the following welding conditions: welding input voltage = 30 V, welding current = 200 A, electrode diameter = 1 mm, electrode-tip/weld distance = 1.3 cm, electrode feed-rate = 10 cm/sec, and gun travel speed = 1 cm/sec

**Figure 6.**  
Spatial distribution of the  
temperature field in the  
weld region over the  
(analyzed) right-portion of  
the MIL A46100 weldment  
at welding times

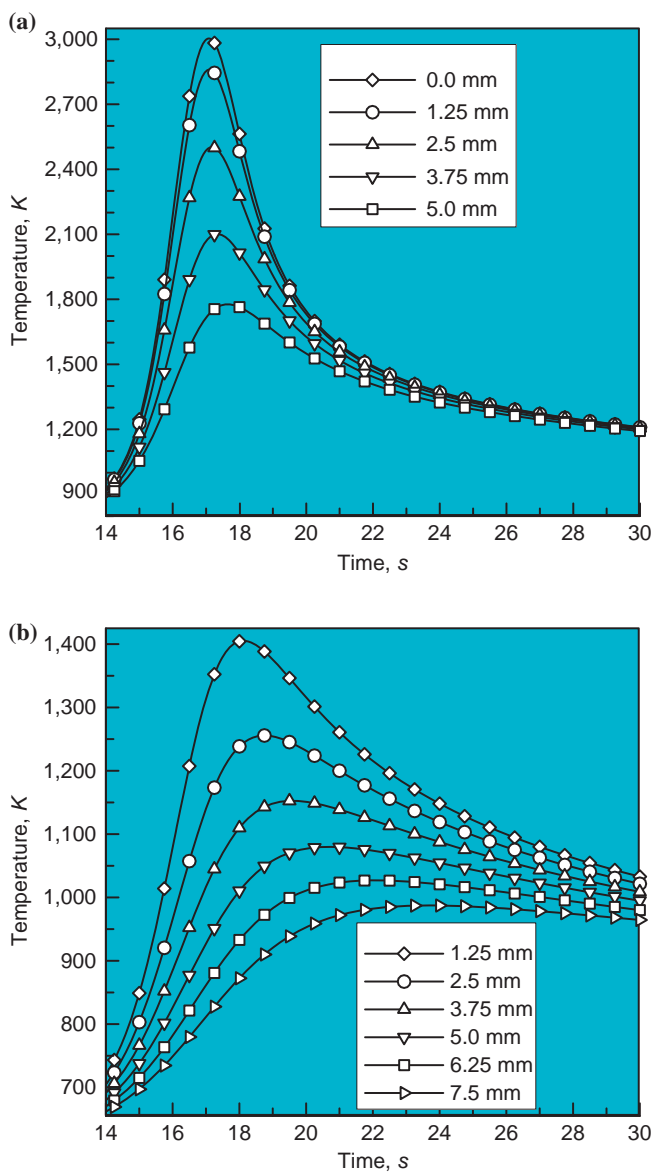


**Notes:** The remaining welding parameters are: welding current = 200 A, electrode diameter = 1 mm, electrode-tip/weld distance = 1.3 cm, electrode feed-rate = 10 cm/sec, and gun travel speed = 1 cm/sec

**Figure 7.**  
The effect of input welding voltage, 30 V in (a) and 35 V in (b), on the spatial distribution of temperature under the identical remaining welding parameters (including the distance traveled by the welding gun)

respectively. As expected, it is seen that an increase in the welding voltage (and thus, in welding power) increases the size of the FZ.

Typical results pertaining to the temporal evolution of temperature at fixed locations within the FZ and HAZ are shown in Figure 8(a)-(b), respectively. The results displayed in Figure 8(a) pertain to the weldment (through-the-thickness) mid-plane within the FZ. Curve labels are used to denote the distance of the material point in question from the weld  $y$ - $z$  symmetry plane. The results displayed in Figure 8(b), on the other hand, also pertain to the weldment mid-plane, but within the HAZ, while the curve labels used in this case, represent the distance of the material point in question from the FZ/HAZ interface. It should be noted that the phase volume fractions in the



**Notes:** (a) Along the workpiece mid-plane within the FZ (the curve labels denote the distance of the subject material point from the weld y-z symmetry plane); and (b) along the workpiece mid-plane within the HAZ (the curve labels denote the distance of the subject material point from the HAZ/FZ interface)

**Figure 8.**  
Temporal evolution  
of temperature

FZ and HAZ, for a larger number of closely spaced material points, are computed in this module and passed to the fourth (microstructure-evolution) module.

Examination of the results displayed in Figure 8(a)-(b) reveals that: first, material points which reside within the FZ experience temperatures in excess of the MIL A46100 liquidus temperature (1,772 K). These points are subjected to a steep rise in temperature, as a result of the arrival of the weld gun, and a relatively steep drop in temperature, as a result of the departure of the weld gun; second, material points which reside within the HAZ experience temperatures which are in excess of the MIL A46100  $A_{c1}$  temperature (982 K) but which are lower than the MIL A46100 liquidus temperature. These points are subjected to a significantly lower heating rate, spend more time at temperatures near the peak temperature and undergo relatively slow cooling; and third, the maximum temperature experienced by the material points, both within the FZ and HAZ, decreases with an increase in distance from the weld centerline.

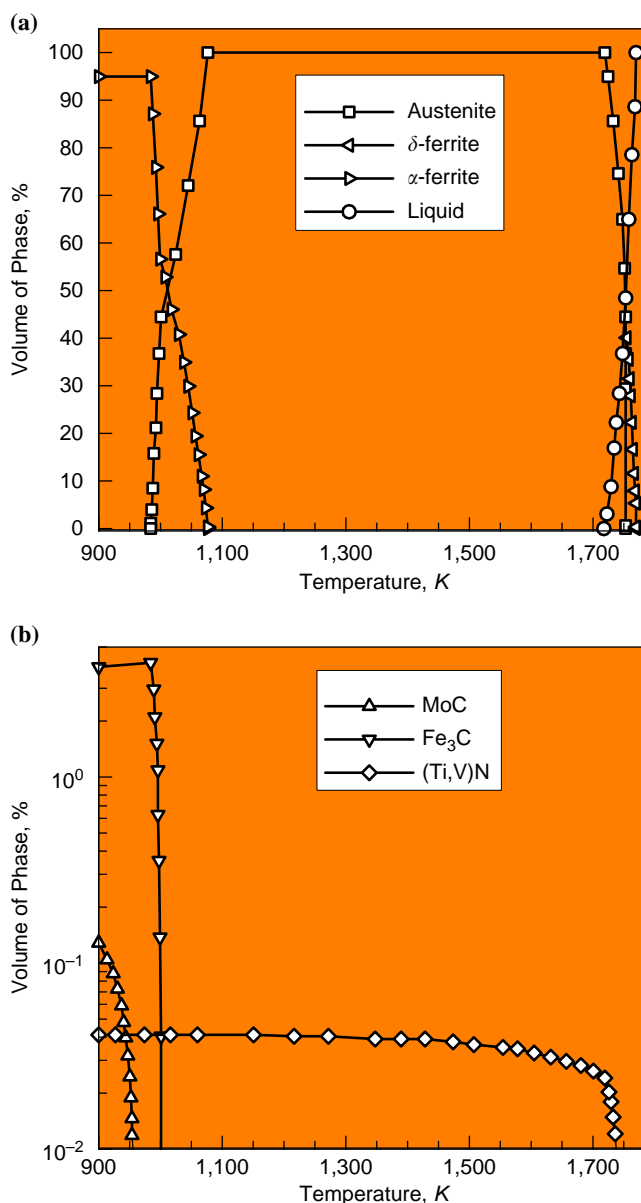
#### 2.4 Microstructure evolution module

The main purpose of this module is to enable predictions of the temporal evolution and spatial distribution of the material microstructure within the weld region. Since GMAW of MIL A46100 is the subject of the present work, the microstructure evolution module is overviewed briefly below while emphasizing the aspects of the module which are specific to this steel. However, before the overview of the module is presented, a brief introduction of MIL A46100 is given.

MIL A46100 falls into the category of air-quenchable, self-tempered, high-hardness, low-alloy martensitic, armor-grade steels. This steel is commonly referred to as a rolled homogeneous armor (RHA) steel, and its chemical composition, material processing, and plate-fabrication routes as well as the resulting as-received material-microstructure and properties are governed by the MIL STD A-46100 specification (US Department of Defense, 1983). The term RHA generally implies that plates of the subject material (used in all metal-armor applications) are produced by hot rolling steel castings. Hot rolling is carried out in such a way that the material microstructure is homogenized while most of the microstructural imperfections/defects are eliminated. Details regarding the chemical composition, typical properties and the weldability and common welding practice associated with MIL A46100 could be found in our recent work (Grujicic *et al.*, 2013a, b). In the same work, details were reported relative to the multi-component equilibrium phase diagram (difficult to visualize/analyze, due to its multi-dimensional character) for MIL A46100, as well as for the “quasi-binary” para-equilibrium (Fe-C) phase diagram (easy to analyze, due to its two-dimensional nature) for this steel. The latter diagram is obtained under the (hypothetical) condition that diffusion of the non-carbon alloying elements (i.e. Mn, Si, Cr, Mo, etc.) does not take place. Examination of the quasi-binary phase diagram established, in Grujicic *et al.* (2013c), that it is quite similar to the true-binary Fe-C phase diagram, except that the values of the characteristic temperatures and concentrations have been slightly modified (due to the presence of non-carbon alloying elements and their low concentration).

As mentioned above, both the multi-component equilibrium phase diagram and the binary para-equilibrium phase diagram have their limitations. That is, the equilibrium phase diagram is difficult to visualize/analyze, while the para-equilibrium phase diagram ignores the phenomenon of non-carbon alloying-element partitioning between different coexisting phases. On the other hand, using various data-extraction mathematical procedures, specific details regarding the chemical composition and the volume fraction of the phases present at a given temperature can be obtained and displayed.

An example of the results obtained by applying such a procedure to MIL A46100 is displayed in Figure 9(a)-(b). The results displayed in this figure show the equilibrium volume fraction of all the phases present, in this steel, at different temperatures and at atmospheric pressure. Examination of the results displayed in Figure 9(a) is used to determine the following characteristic temperatures for MIL A46100: the liquidus



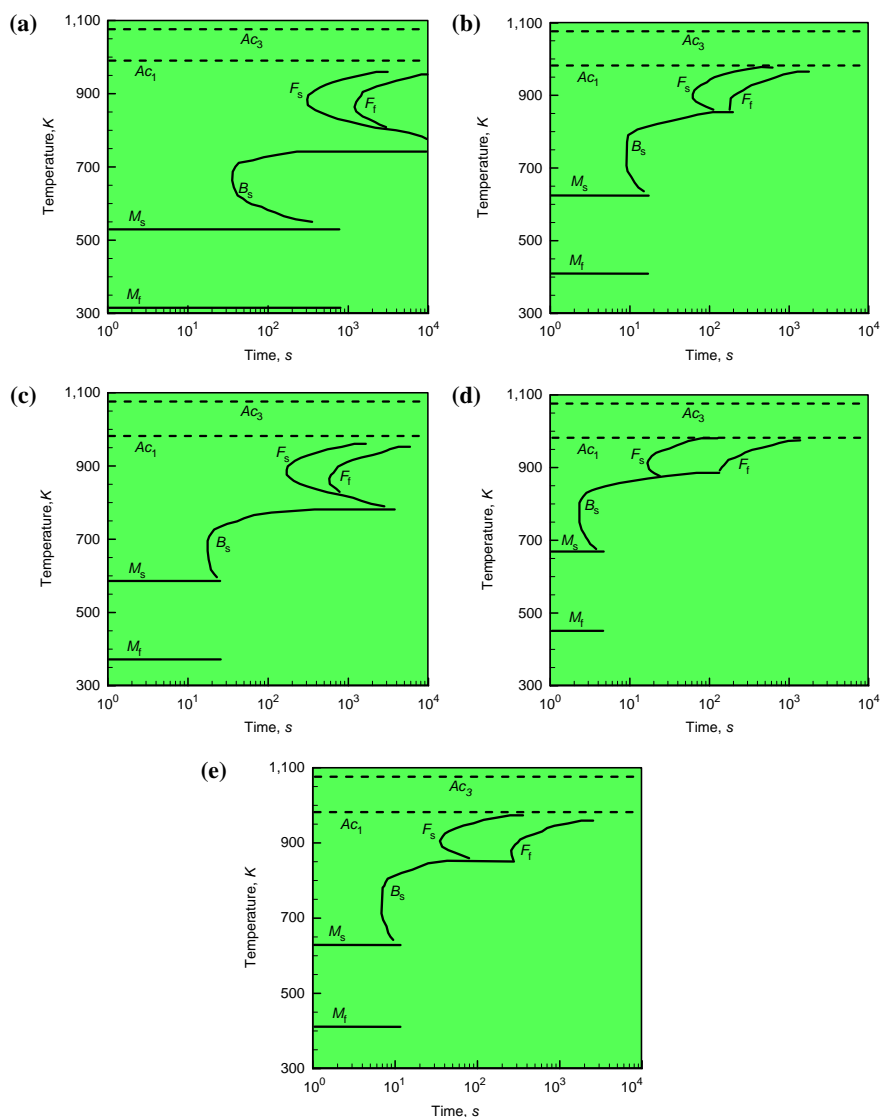
Source: Unfried *et al.* (2009)

**Figure 9.**  
Temperature dependence  
of the equilibrium volume  
fractions of all the phases  
present in MIL A46100  
(at atmospheric pressure)

temperature ( $= 1,772\text{ K}$ ), defined as the temperature at which, during cooling from the melt, the volume fraction of the liquid phase first begins to deviate from 100 percent; the peritectic-transformation temperature ( $= 1,750\text{ K}$ ), defined as the highest temperature at which austenite forms, during cooling; the solidus temperature ( $= 1,720\text{ K}$ ), defined as the temperature at which the liquid phase first vanishes; the  $Ac_3$  temperature ( $= 1,076\text{ K}$ ), defined as the highest temperature at which  $\alpha$ -ferrite forms during cooling; and the  $Ac_1$  temperature ( $= 982\text{ K}$ ), defined as the highest temperature at which austenite is still present, during cooling. Furthermore, examination of the results displayed in Figure 9(b) reveals that: (Ti,V)(N,C) primary precipitates first appear at temperatures slightly above the solidus temperature, due to the associated high super-saturation of the residual liquid with the primary precipitate constituent elements; the precipitate volume fraction does not experience a significant change during subsequent cooling; as expected, cementite precipitates begins to form during cooling at a temperature in the  $Ac_1$ - $Ac_3$  range; and as expected, the formation of alloy-carbide precipitates, like MoC, begins at temperatures below  $Ac_1$ .

In low-alloy steels, like MIL A46100, austenite (a high-temperature  $\gamma$ -phase with face-centered-cubic, FCC crystal structure) transforms, during cooling, into one or more low-temperature ferrite (a low-temperature  $\alpha$ -phase with body-centered-cubic, BCC crystal structure) based phases/micro-constituents. Some, but not all of these phase transformations are predicted by the equilibrium phase diagram. Those which are not predicted by the phase diagrams are associated with non-equilibrium meta-stable, crystallographic phases/microconstituents. The formation of these phases is the result of non-equilibrium finite cooling rate conditions, the conditions which hamper the formation of the equilibrium phase. To graphically represent the kinetics of formation of the non-crystalline phases/microconstituents, other material-specific time-based diagrams are used (in place of the equilibrium phase diagram). One of these diagrams is the so-called "time-temperature-transformation" (TTT) diagram. Figure 10(a)-(e) show a series of MIL A46100 TTT diagrams. Each of these TTT diagrams is associated with a specific temperature at which the steel was austenitized until the equilibrium volume fraction was reached. The TTT diagrams reveal the kinetics of various austenite decomposition phase transformations under a very specific cooling history from the austenitization temperature. That is, the material is quenched to a given temperature (below  $Ac_3$ ) and then the temperature is held constant until the rate of further austenite-decomposition becomes negligibly small. The TTT diagrams have been traditionally derived using purely experimental means. However, due to recent advances in the computational analyses of austenite decomposition, the TTT diagrams, for many steels, can be generated analytically/numerically. In fact, the TTT diagrams displayed in Figure 10(a)-(e) were originally generated by Unfried *et al.* (2009) using a proprietary computer code.

Examination of the TTT diagrams displayed in Figure 10(a)-(e) reveals the presence of three (complete or partial) C-shaped curves. The two high-temperature curves labeled  $F_s$  and  $F_f$  represent, respectively, the loci of the incubation times (times prior to the commencement of the particular phase transformation) for the allotriomorphic ferrite and acicular/Widmanstätten ferrite. Allotriomorphic ferrite is a variation of ferrite possessing a featureless external morphology which does not reflect the symmetry of the associated underlying crystalline structure. Acicular/Widmanstätten ferrite, on the other hand, is a version of ferrite possessing an acicular/lenticular-plate morphology which grows into the untransformed austenite from the austenite/austenite grain boundaries and/or allotriomorphic-ferrite/austenite interfaces. The lower C-shaped



**Notes:** (a) 993 K; (b) 1003 K; (c) 1053 K; (d) 1,076 K; and (e) 1,330 K. Symbols  $F_s$ ,  $F_f$  and  $B_s$  are used to denote the locus of the temperature vs time conditions at which austenite begins to transform, respectively, into allotriomorphic ferrite, acicular ferrite and bainite. Symbols  $Ac_3$ ,  $Ac_1$ ,  $M_s$  and  $M_f$  have their common meanings (please see text for details)  
**Source:** Unfried *et al.* (2009)

**Figure 10.**  
 The time-temperature-transformation (TTT) diagrams for MIL A46100 steel equilibrated initially

curve in Figure 10(a)-(e),  $B_s$ , is associated with the displacive bainitic phase transformation. This transformation produces a lath or acicular-shaped bainitic phase and, during this transformation, atomic diffusion of iron and alloying elements other than carbon is suppressed. Two low-temperature lines, marked as  $M_s$  and  $M_f$  in Figure 10(a)-(e), define, respectively, the temperatures at which, during cooling, displacive/diffusionless

austenite-to-martensitic phase transformation starts and finishes. The product of this transformation, martensite, is a solid solution with a highly distorted (due to high levels of carbon super-saturation) body-centered tetragonal crystal structure and acicular morphology. Two high-temperature lines, marked as  $Ac_1$  and  $Ac_3$  in Figure 10(a)-(e), correspond to the previously mentioned equilibrium characteristic temperature associated with austenite decomposition during cooling.

Another type of diagram which is used to display the kinetics of austenite decomposition during cooling is the so-called CCT (Continuous Cooling Transformation) diagram. In the case of CCT diagrams, the thermal histories associated with austenite cooling from a fixed austenitizing temperature (the histories which are used to determine the locus of the points associated with the start and the finish of the aforementioned phase transformations) are characterized by constant cooling rates. An example of the CCT diagram for MIL A46100 is shown in Figure 11. The procedure for constructing this diagram from the TTT diagram, associated with the same austenitizing temperature, could be found in our previous work (Grujicic *et al.*, 2013b). It should be noted that both TTT and CCT curves are shown in Figure 11 and, for improved clarity, the TTT curves are denoted in this figure using dashed lines. For the same reason, the resulting CCT curves are drawn as heavy solid lines, while representative constant-rate cooling curves are denoted as light solid lines. It should be noted that, the  $M_s$  and  $M_f$  horizontal lines in Figure 11 coincide with their TTT counterparts. This result is expected considering the fact that the martensitic transformation is of an athermal character and, hence, is not affected by the details of the material cooling history (down to room temperature).

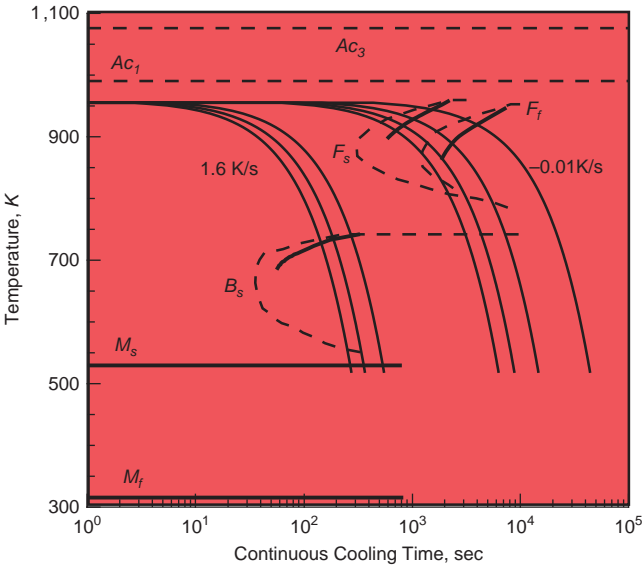
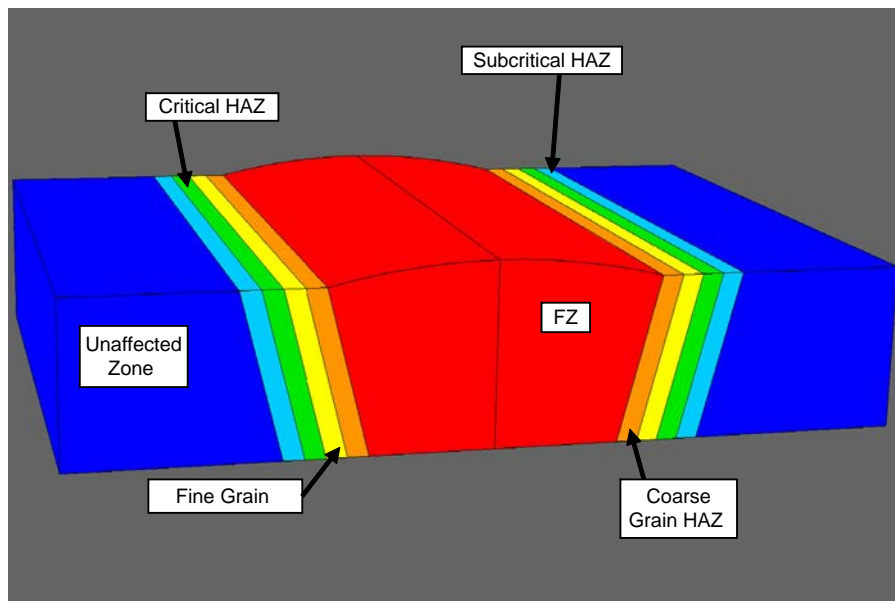


**Figure 11.**  
MIL A46100 continuous-cooling-transformation (CCT) diagram corresponding to the TTT diagram displayed in Figure 10 (a)

**Notes:** CCT curves and the  $M_s$  and  $M_f$  temperature lines are denoted using heavy solid lines, while representative cooling curves are shown as light solid lines. The TTT curves and the  $Ac_1$  and  $Ac_3$  temperature lines are denoted using dashed lines

As schematically shown in Figure 12, the GMAW weld region consists of the FZ (i.e. the solidified weld pool) and the surrounding HAZ. It is further seen that the HAZ itself is divided into several sub-zones. Moving outward from the weld centerline, the following HAZ sub-zones are generally found in GMAW welds: first, the coarse-grained sub-zone, which mainly contains martensite. The prior austenite grain size in this region is quite large due to steel exposure to very high temperatures (within the single-phase austenite region); second, the fine-grained sub-zone, which contains a mixture of martensite and bainite, formed during cooling, from austenite with a relatively smaller grain size due to its exposure to lower temperatures (within the single-phase austenite region); third, the so-called inter-critical sub-zone, within which the base-metal is exposed to temperatures sufficiently high, and/or time sufficiently long, to enable the formation of austenite. However, the combination of the high temperature and the long exposure time is insufficient to yield complete austenitization. Consequently, this sub-zone contains both non-austenite phases (i.e. ferrite and alloy-carbides) present at the highest temperature to which this sub-zone was exposed and the products of austenite decomposition during cooling (i.e. martensite, bainite, ferrite); and fourth, the so-called sub-critical zone, within which the material was never exposed to a temperature sufficiently high, and/or to times sufficiently long, to result in the formation of austenite. However, high temperature exposure of the material in this subzone typically causes martensite tempering (i.e. formation of a mixture of ferrite and fine carbide particles).

It should be first recognized that the same computational procedure used to construct the TTT and CCT diagrams could also be used to predict the incubation times for austenite decomposition into different crystal phases/microconstituents, under an arbitrary thermal history. However, additional modeling and simulation procedures are needed to predict further progress of these austenite-decomposition reactions (and the corresponding volume fractions of the transformation products).



**Notes:** FZ, fusion zone; HAZ, heat-affected zone

**Figure 12.**  
A schematic of the  
typical GMAW process  
zones and sub-zones

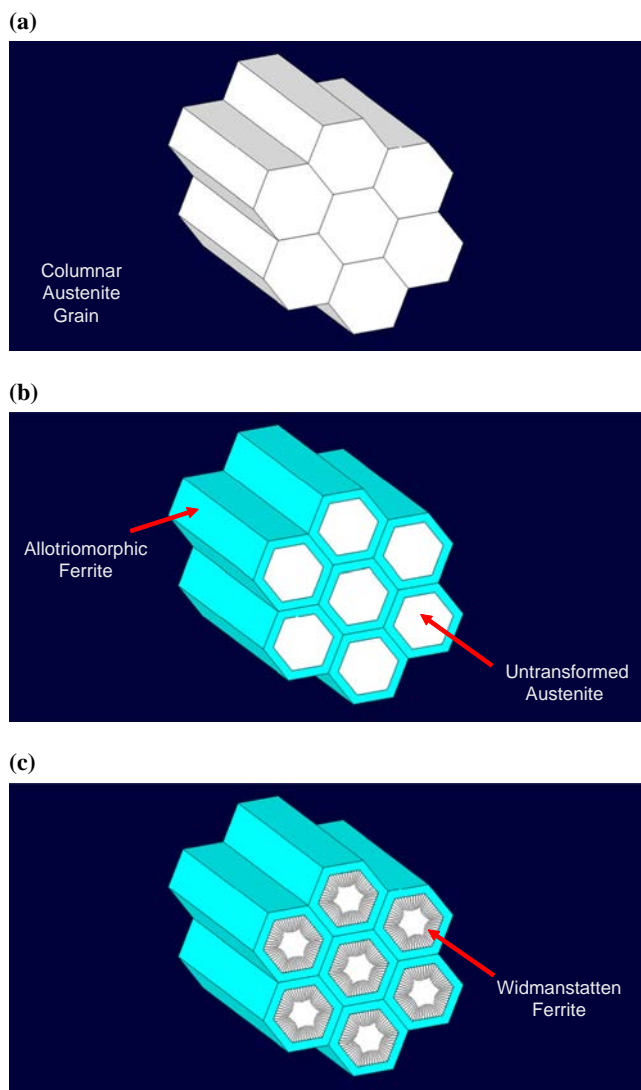
Such procedures are developed in the microstructure-evolution module, and are overviewed briefly, in the remainder of this and the subsequent section. Due to substantially different thermal histories of the two weld zones, separate models are developed for the material points residing in the FZ and the HAZ. Thermal history of the material points within the FZ is dominated by the continuous cooling of austenite (formed from the liquid phase during solidification). On the other hand, thermal history of the material points within the HAZ involves initial heating of the as-received martensitic microstructure and subsequent cooling of the austenite phase (formed from the martensitic phase during heating).

As established earlier, depending on the thermal history, high-temperature austenite, present within the FZ, can transform into one or a mixture of the following phases: allotriomorphic ferrite, acicular ferrite, bainite and/or martensite. A detailed description of the procedures for computing the final volume fractions of these austenite-decomposition product phases could be found in our prior work (Grujicic *et al.*, 2013c). Only a synopsis of these procedures is provided hereafter.

The kinetics of austenite decomposition into allotriomorphic ferrite is modeled in the following way: first, it was recognized that this is a heterogeneous type of phase transformation since allotriomorphic ferrite forms preferentially at the austenite grain boundaries; second, while modeling (columnar) austenite grains as parallel equal-sized hexagonal prisms with their axis aligned with the local maximum thermal gradient, while assuming that a relationship is established between the hexagon edge-length and the solidification rate. A schematic of the transverse section of the purely austenitic honeycomb-type microstructure is depicted in Figure 13(a); third, the incubation times for nucleation of the allotriomorphic ferrite, under arbitrary cooling history conditions, is determined using the same computational procedure as that employed in the construction of the TTT and CCT diagrams; fourth, growth of the allotriomorphic ferrite is modeled under the following simplifying (but physically justified) assumptions: there is a parabolic relationship between the allotriomorphic-ferrite thickness growth rate and the current ferrite-plate thickness; and the allotriomorphic ferrite plate thickness can be obtained by integrating its growth rate over the arbitrary thermal history. Figure 13(b) displays a schematic of the idealized microstructure in which the grain-boundary portion of austenite is partially transformed into allotriomorphic ferrite; fifth, the transformation in question is assumed to take place under para-equilibrium conditions in which non-carbon elements are assumed not to partition between the phases; and sixth, austenite → allotriomorphic ferrite transformation is assumed to cease once kinetically superior austenite → Widmanstätten ferrite or austenite → bainite phase transformations initiate.

The onset of austenite → Widmanstätten ferrite phase transformation is again determined using the procedure employed during construction of the corresponding portions of the TTT and CCT diagrams. As far as the growth of the nucleated Widmanstätten ferrite is concerned, its kinetic model is derived under the following physically based simplifying assumptions: the growth rate of the Widmanstätten ferrite is assumed to be controlled by the rate of lengthening of this lens-shaped phase in a direction normal to the local allotriomorphic ferrite/austenite interface; and the rate of the austenite → Widmanstätten-ferrite phase transformation is affected not only by the para-equilibrium condition present at the ferrite advancing front, and the associated carbon diffusion from this front into the untransformed austenite, but also by the displacive character of the austenite → Widmanstätten ferrite phase transformation.

A simple schematic of partially transformed austenite grains, into a mixture of allotriomorphic and acicular ferrites, is depicted in Figure 13(c). The figure clearly



**Notes:** (a) Untransformed austenite; (b) austenite partially transformed into allotriomorphic ferrite; and (c) austenite partially transformed into allotriomorphic and Widmanstatten ferrite

**Figure 13.**  
Schematic representations  
of the columnar-grain  
microstructure

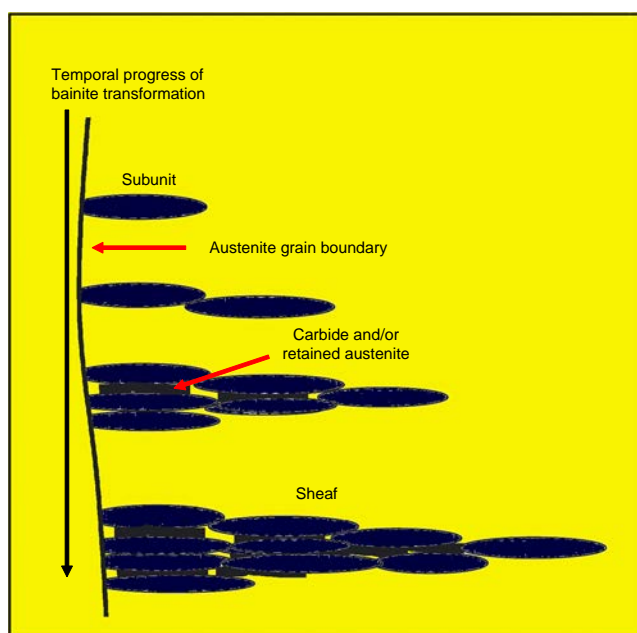
shows the presence of prior austenite grain-boundary regions which have been transformed into allotriomorphic ferrite, as well as lenticular-shaped Widmanstatten plates advancing from the allotriomorphic ferrite/austenite interfaces toward the untransformed austenite grain centers.

While the austenite→bainite phase-transformation is of a displacive character, its progress is controlled by carbon diffusion into the untransformed austenite matrix.

This phase transformation is generally assumed to involve the following three distinct processes (Bhadeshia *et al.*, 1985; Jones and Bhadeshia, 1997; Matsuda and Bhadeshia, 2004):

- Nucleation and lengthening of bainite platelets (commonly referred to as sub-units) at austenite grain boundaries and phase interfaces. Upon reaching a critical size, lengthening of the bainite sub-units is arrested by the plastic deformation accumulated within the surrounding austenite.
- The transformation then proceeds by nucleation of new sub-units ahead of the arrested ones. The newly formed sub-units also become arrested and this sequence of processes continues.
- The result of the sequential nucleation of bainite sub-units is the formation of unit clusters commonly referred to as “sheaves.” It is the rate of lengthening of the sheaves which is believed to control the overall progress of the austenite → bainite phase transformation. A schematic of this bainite-formation mechanism is depicted in Figure 14.

The onset of the austenite → bainite phase transformation is determined within the GMAW microstructure-evolution module by using the same procedure as that employed in the construction of the corresponding sections of the TTT and CCT diagrams. The subsequent growth of bainite is modeled within the module by using the approach proposed by Matsuda and Bhadeshia (2004) in which the rate of bainitic transformation, for each of the three processes described above, is expressed as a function of time, temperature, chemical composition (and austenite grain size).



Source: Matsuda and Bhadeshia (2004)

**Figure 14.** Schematic of the bainite growth mechanism via the nucleation of sub-units, their growth and arrest, and subsequent autocatalytic nucleation of new sub-units (resulting in the formation of sub-unit clusters commonly referred to as sheaves)

When the temperature of the remaining untransformed austenite falls below the  $M_s$  temperature, operation of all the aforementioned austenite-decomposition phase-transformations is terminated by the kinetically superior diffusionless austenite  $\rightarrow$  martensite phase transformation. The martensitic transformation is of an athermal nature, i.e. its progress is not a function of time. Rather, the extent of this transformation is controlled by the lowest temperature that the untransformed austenite was ever subjected to. According to the results displayed in Figure 10(a)-(e), the  $M_f$  temperature is above the room temperature. Consequently, one would expect a complete remaining austenite transformation during cooling to room temperature. This (zero-retained austenite volume fraction) condition is assumed within the GMAW microstructure-evolution module. Within the module, the growth kinetics of martensite is not analyzed explicitly. Rather, the room-temperature volume fraction of martensite is computed as a difference between 1.0 and the sum of volume fractions of all the room-temperature phases.

Other potential phases present at room temperature are not related directly to decomposition of austenite, but rather the results of the precipitation reactions which take place once the solubility limit for austenite is exceeded, during cooling. In MIL A46100, these phases generally include (Ti,V) N and MoC. The equilibrium room-temperature volume fractions of these phases, however, are quite small (and the actual volume fractions are even smaller). Consequently, the role of these phases within the GMAW microstructure-evolution module is ignored.

As explained earlier, material points within the HAZ are subjected to more complicated thermal histories which include both heating and cooling portions. The HAZ is operationally defined as a region surrounding the FZ within which these thermal histories cause noticeable and significant changes in the weldment-material microstructure and properties. Within the microstructure-evolution module, changes in the HAZ material microstructure during heating and cooling portions of the thermal history are analyzed separately.

MIL A46100 in its as-received condition typically possesses an auto-tempered martensitic microstructure. The extent of changes in this microstructure within the HAZ is mainly a function of the maximum-exposure temperature (as well as the exposure time of the material to the highest temperatures). Specifically, if the maximum-exposure temperature never exceeds  $A_{c1}$ , the only microstructural changes expected are those associated with (additional) tempering of martensite. The outcome of these microstructural changes is the formation of ferrite and, initially,  $\epsilon$ -carbide (or, finally, alloyed cementite). On the other hand, when the maximum-exposure temperature exceeds  $A_{c1}$ , formation of austenite at the prior-austenite grain boundary junctions takes place. A schematic of this martensite  $\rightarrow$  austenite phase transformation is depicted in Figure 15(a)-(b), in which elongated prior-austenite grains are shown in order to reveal the effect of hot-rolling on the material microstructure.

To model the carbide-precipitation reactions associated with martensite tempering and phase transformations associated with austenite formation from martensite, analogous approaches are used in this study. That is, in both cases it is assumed that the processes in question, involve nucleation and subsequent growth of the product phases (under para-equilibrium conditions). The progress of these processes is represented mathematically by modifying the conventional Kolmogorov-Johnson-Mehl-Avrami isothermal relation (Kruger, 1993) for the case of arbitrary thermal history.

In the case of maximum-exposure temperatures not exceeding  $A_{c1}$ , martensite tempering simply continues (at a progressively lower rate) during cooling to room

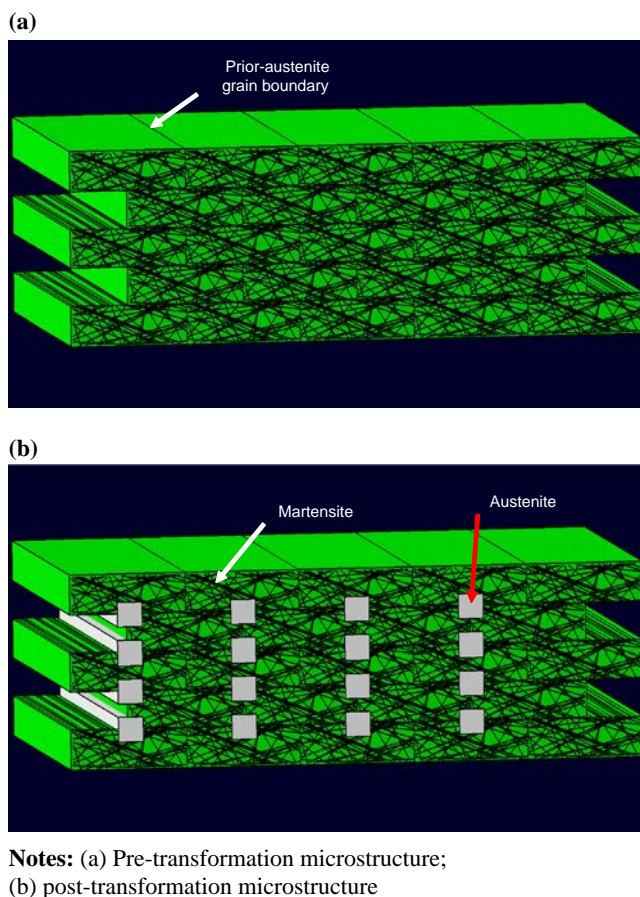


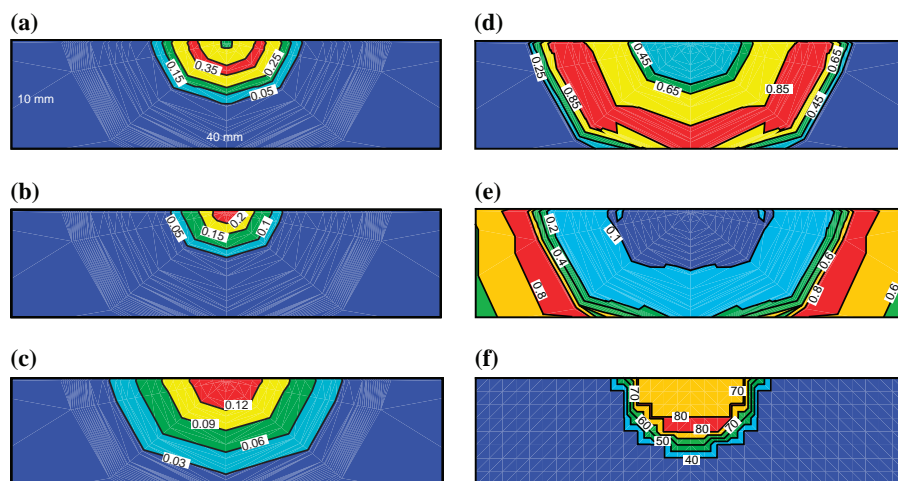
**Figure 15.**  
A schematic of austenite formation at the prior-austenite grain-boundary junctions within a fully-martensitic as-hot-rolled microstructure during super- $A_{c1}$  thermal exposure

temperature. In this case, the same approach as that described for the heating portion of the thermal cycle can be used to model additional martensite-tempering. As far as the case of a super- $A_{c1}$  maximum-exposure temperature is concerned, austenite formed during heating undergoes decomposition, during subsequent cooling to room temperature. The associated austenite-decomposition phase transformations are analyzed using the same approach as the one developed in the case of FZ, while recognizing the following differences between the two cases: austenite, formed within the  $A_{c1}$ - $A_{c3}$  temperature range, possesses a different chemical composition than its counterpart in the FZ. Specifically, due to the hypo-eutectoid character of MIL A46100, austenite formed in this temperature range is enriched on alloying elements relative to the nominal chemical composition of MIL A46100; consequently, as supported by the results displayed in Figure 10(a)-(e), austenite is less likely to transform into one of its high-temperature decomposition products, i.e. allotriomorphic ferrite and/or Widmanstätten ferrite; and during austenite decomposition within HAZ, austenite/martensite (and, perhaps, austenite/bainite) interfaces may already exist at the onset of cooling and, hence, martensite/bainite nucleation is not required and the overall progress of austenite to martensite/bainite transformations becomes controlled by the growth, rather than nucleation, kinetics.

Except for a few minor reparameterizations regarding the kinetics of bainitic transformation, no improvements are made in the current rendition of the microstructure-evolution module.

Examples of the results yielded by the microstructure evolution module are depicted in Figure 16(a)-(f). These results are obtained for MIL A46100, initially in the as-hot-rolled and self-tempered martensitic state, under the following GMAW process conditions: input welding voltage = 30 V, welding current = 200 A, electrode diameter = 1 mm, electrode-tip/weld distance = 1.3 cm, electrode feed-rate = 10 cm/s, and gun travel speed = 1 cm/s. In Figure 16(a)-(e), the spatial distributions of phase volume fractions over a transverse section of the weld and the workpiece region adjacent to the weld are presented for: allotriomorphic ferrite; Widmanstätten ferrite; bainite; freshly formed martensite; and tempered martensite, respectively. In Figure 16(f), the corresponding spatial distribution of the prior-austenite grain size is shown.

Examination of the results displayed in Figure 16(a)-(f) reveals that: first, allotriomorphic ferrite and Widmanstätten ferrite are both present only within the FZ, Figure 16(a)-(b). This observation is fully consistent with the fact that the material within this region is initially subjected to temperatures substantially higher than the material liquidus temperature and, consequently, is associated with a long cooling time. Furthermore, the material within the FZ possesses relatively low hardenability (the ease of transformation of austenite into martensite), since austenite chemical composition is nearly identical to that of the alloy itself; second, the volume fraction of freshly formed martensite within the FZ is fairly small (<30 vol. %, Figure 16(d)). This finding is to be expected, considering the relatively low cooling rates and the relatively low hardenability of austenite found in this weld region. As one crosses the FZ/HAZ interface and enters the HAZ, the volume fraction of freshly formed martensite first increases (to a value in excess of 85 vol. percent) and then decreases (to a value of ca. 10 vol. %). Once the HAZ/unaffected-material boundary is crossed the volume fraction of the freshly formed martensite drops to zero. This spatial distribution of the volume fraction of freshly



**Notes:** (a) Allotriomorphic ferrite; (b) Widmanstätten ferrite; (c) bainite; (d) freshly formed martensite; (e) tempered martensite; and (f) grain size (in microns) over a transverse section of the weld and the workpiece region adjacent to the weld

**Figure 16.**  
Spatial distribution of  
phase volume fractions

formed martensite is a consequence of a trade-off between the amount of austenite available to transform into martensite and the hardenability of austenite. Specifically, in the HAZ regions which were exposed to temperatures above  $Ac_3$ , full austenitization is assumed to take place. However, this austenite possesses low hardenability. On the other hand, as one enters the inter-critical region, within which the maximum exposure temperature is between  $Ac_1$  and  $Ac_3$ , austenitization becomes incomplete but the attendant austenite possesses higher hardenability. Consequently, as the maximum exposure temperature decreases from  $Ac_3$  to  $Ac_1$ , the volume fraction of the freshly formed martensite first increases (due to the dominating effect of the increased austenite hardenability), then passes through a peak value and finally decreases (due to a lower volume fraction of austenite available for transformation to martensite). When the maximum exposure temperature is below  $Ac_1$ , no austenitization takes place during heating and, hence, austenite  $\rightarrow$  (freshly formed) martensite phase transformation takes place; third, since the austenite  $\rightarrow$  bainite phase transformation is mainly competing with the austenite  $\rightarrow$  (freshly formed) martensite phase transformation, variation of the volume fraction of bainite throughout the FZ and within the HAZ (as a function of distance from the FZ/HAZ interface), Figure 16(c), is a mere reflection of the outcome of this competition; fourth, tempered martensite is not present in the FZ, or within the portion of the HAZ which was fully austenitized, Figure 16(e). In the remainder of the HAZ, volume fraction of tempered martensite increases with distance from the FZ/HAZ interface and ultimately reaches a value of 100 percent, at a locus of the HAZ points with a maximum exposure temperature of  $Ac_1$ ; and fifth, as one moves toward the top-center point of the FZ, the grain size first continuously increases from its initial value (40 microns), to a value of  $\sim 80$  microns near the HAZ/FZ interface, Figure 16(f). As one enters the FZ, the grain size first drops (the “chill-zone” effect) and then continues to increase toward the final value of  $\sim 70$  microns.

### 2.5 Microstructure/property relationship module

The main purpose of this module is to establish functional relationships between the material microstructure (quantified primarily by the corresponding phase/micro-constituent volume fractions) and the material mechanical properties (primarily hardness/strength). These relationships are next used to determine spatial distribution of the material properties throughout different weld regions. In the rendition of the microstructure/property relationship module reported by Grujicic *et al.* (2013c), a very simple procedure is used to calculate the local hardness of the material within the weld region. This procedure is based on the following assumptions: local hardness is the result of the weighted average of all attendant phase/micro-constituent hardnesses; hardness of each phase/micro-constituent can be set to a constant prototypical value, as obtained experimentally using micro-/nano-indentation tests; and contribution of the prior-austenite grain size can be accounted for using the conventional Hall-Petch relationship (Gore *et al.*, 1989).

As mentioned earlier, the main objective of the present work is to improve the predictive capabilities of the microstructure/property relationship module with respect to the spatial distribution of the material properties throughout different portions of the weld. The specific improvements in the GMAW microstructure/property module proposed in the present work are carried out using the following three-step procedure:

- (1) first, the main contributions to the material strength within different portions of the weld zones are identified and the governing equations for the corresponding strengthening mechanisms assembled and parameterized;

- (2) a superposition scheme is then developed in order to assess the combined effect of different strengthening mechanisms; and
- (3) finally, a functional relationship is established between the material strength and hardness so that spatial distribution of the material hardness within the weld can be determined.

Such a distribution can next be compared with its experimental counterpart in order to validate the multi-physics GMAW process model.

After analyzing the crystal structure, chemical composition, internal sub-structure and external morphology of the attendant phases/micro-constituents, the following main strength contributors are identified, modeled and parameterized: intrinsic (i.e. Peierls barrier control) strength of the phases/micro-constituents; solid solution strengthening; alloy-carbide/cementite precipitation hardening; dislocation substructure-based strengthening; and strengthening by grain boundaries and phase interfaces.

This contribution to the local material strength is identical to the one accounted for in the original version of the microstructure/property relationship module (Grujicic *et al.*, 2013c) and, hence, will not be discussed here.

This type of strengthening is assumed to be controlled by the elastic (size and modulus mismatch type of) interactions between the solute atoms and dislocations (Fleischer, 1963). To assess the contribution of this mechanism to the material strength, the statistical approach of Labusch (1970) is utilized, which accounts for the distribution of the atom/dislocation interaction forces and distances. According to this approach, the critical resolved shear stress required for dislocation glide, in phase  $\alpha$ , is increased by the solid solution strengthening effects of the alloying element  $i$  by:

$$\Delta\tau_{SS,i}^{\alpha} = Z_i^{\alpha} G^{\alpha} \left( |\varepsilon_{G,i}| + \beta_i^{\alpha} |\varepsilon_a| \right)^{4/3} (c_i^{\alpha})^{2/3} \quad (2)$$

where  $Z_i^{\alpha}$  and  $\beta_i^{\alpha}$  are phase/species dependent material parameters, while  $G^{\alpha}$  is the phase shear modulus,  $\varepsilon_{G,i}$  and  $\varepsilon_a$  are the modulus and size misfit parameters and  $c_i^{\alpha}$  is the concentration of the alloying species in question. Parameters  $Z_i^{\alpha}$  and  $\beta_i^{\alpha}$  are taken from Wise (1998),  $G^{\alpha}$  values are taken from our previous work (Grujicic *et al.*, 2013c), values for  $\varepsilon_{G,i}$  and  $\varepsilon_a$  are taken from Wise (1998) and  $c_i^{\alpha}$  for each alloying species, in each phase, is obtained from the results yielded by the microstructure-evolution module.

MIL A46100 derives its strength from lightly tempered martensite. However, the high temperature exposure of the HAZ material, as mentioned earlier, can give rise to further tempering of martensite and the associated formation of alloy-carbide/cementite. In this case, as the strength of tempered martensite decreases, the contribution of alloy-carbide/cementite precipitates to the material strength increases. Consequently, to properly model the strength of the material within the HAZ, the contribution of precipitation hardening mechanism(s) must be taken into account. This is done in the present work.

Precipitation hardening results from the increased resistance gliding dislocations experience as a result of their interactions with precipitates. The extent of precipitate hardening is controlled by factors such as precipitate size, volume fraction, number density and chemical/mechanical properties, as well as by the state of coherency at the precipitate/matrix interfaces. In general, gliding dislocations can overcome precipitates in two different ways:

- (1) by precipitate shearing/cutting, the process which increases precipitate/matrix interfacial area and leads to the formation of interfacial ledges, stacking faults and anti-phase boundaries, (in the case of ordered crystalline precipitates); and

- (2) by looping around the precipitates, the process which leaves behind dislocation loops surrounding the precipitates and increases the effective size of the precipitates.

The critical resolved shear stress required for precipitate shearing increases as the size of the precipitates increases. On the other hand, at a given volume fraction of the precipitates, the critical resolved shear stress for precipitate-bypass via the looping mechanism decreases with an increase in the precipitate size. Consequently: precipitate shearing controls the extent of precipitation hardening for small precipitates; dislocation looping around the precipitates controls precipitate hardening at large precipitate sizes; and there is a critical precipitate size, at which, the extent of precipitate hardening is the highest. The degree of precipitate hardening associated with the shearing process depends on the nature and the extent of phenomena/processes (e.g. precipitate/matrix interfacial energy, character/magnitude of the stress-free eigen-strain of coherent precipitates, the extent of precipitate/matrix elastic-modulus mismatch, the stacking fault energy, the anti-phase boundary energy, etc.) responsible for the resulting increase in the critical resolved shear stress required for dislocation glide. Considering the fact that incoherent alloy-carbide/cementite precipitates are primarily found in MIL A46100, and following the standard practice (e.g. Wise, 1998), it is assumed, in the present work, that the shearing mode of the precipitate hardening process is controlled by the elastic-modulus mismatch between the matrix and the precipitates. Consequently, the associated increase in the critical resolved shear stress for dislocation glide is defined as:

$$\Delta\tau_{p, shear} = 0.65 \frac{Gb}{(L - 2r)} \left( \frac{G_p r}{2\pi Gb} \right) \quad (3)$$

where subscript  $p$  denotes a quantity associated with a precipitate phase,  $b$  is the Burgers vector,  $L$  is the inter-precipitate spacing along the dislocation line, and  $r$  is the precipitate effective radius. All the parameters appearing in Equation (3) were obtained from the following sources (Grujicic, 1989; Grujicic *et al.*, 1992, 1997, 2013c; Wells *et al.*, 1992; Wise, 1998).

As far as the critical resolved shear stress required for precipitate-bypass by the looping mechanism, it is quantified using the Orowan-Ashby approach (Ashby, 1969), which is based on the assessment of the stress required to bend a dislocation segment into a semi-circular shape with a radius equal to the precipitate half-distance along the dislocation line as:

$$\Delta\tau_{p, loop} = 1.68 \frac{Gb}{2\pi\sqrt{1-\nu}(L - 2r)} \ln\left(\frac{2r}{r_0}\right) \quad (4)$$

where  $\nu$  is the Poisson's ratio and  $r_0$  ( $= b$ ) is the dislocation-core radius. Again, all the parameters appearing in Equation (4) were obtained from the following sources (Grujicic, 1989; Grujicic *et al.*, 1992, 1997, 2013c; Wells *et al.*, 1992; Wise, 1998).

Due to a large shape change (i.e. lattice-invariant shear strain) accompanying austenite  $\rightarrow$  martensite phase transformation, plastic relaxation takes place, both within the growing martensitic phase and within the adjacent austenite phase. Consequently, freshly formed martensite typically contains a large density of dislocations. Since dislocations act as obstacles to other dislocations, dislocation glide requires an increase

in the critical resolved shear stress and, hence, material strength is increased. The extent of this strengthening is a function of the transformation temperature since this temperature affects the strength of, and the extent of plastic relaxation in, the transforming austenite. Following Takahashi and Bhadeshia (1990), the following functional relationship is used between the transformation-induced dislocation density,  $\rho$ , and the transformation temperature,  $T$ :

$$\log(\rho) = 9.2848 + \frac{6,880.73}{T} - \frac{1,780,360}{T^2} \quad (5)$$

The associated increase in the critical resolved shear stress is assessed using the approach of Keh and Weissman (1963):

$$\Delta\tau_\rho = 0.38Gb\sqrt{\rho} \quad (6)$$

It should be noted that Equation (5) defines the dislocation density within freshly formed martensite. However, martensite tempering, taking place predominantly within the HAZ, is accompanied by dislocation recovery, a process which rearranges and (partially) annihilates dislocations (causing a loss in the material strength). The extent of recovery-induced loss of strength increases with increases in tempering temperature and time. This loss is assessed in the present work by modeling the relationship originally proposed by Leslie *et al.* (1963) as:

$$\Delta\tau_{\rho, \text{ recovery}} = -a \log(t - t_{\text{incubation}}) \quad (7)$$

where  $a$  and  $t_{\text{incubation}}$  are material-dependent Arrhenius-type functions, as defined by Leslie *et al.* (1963).

In contrast to the previously analyzed obstacles to dislocation glide (i.e. substitutional/interstitial alloying atoms, precipitates and “forest” dislocations), grain boundaries and phase interfaces act as impenetrable barriers to dislocation glide. Consequently, during plastic deformation, dislocation pile-ups are formed at these boundaries and interfaces, and the subsequent plastic deformation depends on the nucleation and glide of dislocations in the adjacent grains/phase-particulates (promoted by the stress-concentration effects arising from the dislocation pile-ups). In general, the larger the grain/phase-particulate size, the larger is the dislocation pile-up that can be accommodated, the larger are the pile-up induced stress-concentration effects and the lower is the applied stress at which new dislocations are nucleated. In other words, material strength decreases with a increase in the grain/phase-particulate size. This effect is accounted for in the present work using the Hall-Petch relation as:

$$\Delta\tau_{\text{boundary}} = k^z (d^z)^{-1/2} \quad (8)$$

where  $k^z$  is the phase/micro-constituent dependent parameter and  $d^z$  is the average grain/phase-particulate diameter.

Based on the results and discussion presented earlier, it is evident that there are different grain boundaries and phase interfaces in MIL A46100 (e.g. prior austenite grain boundaries, martensite lath boundaries, bainitic sheave boundaries and the associated two-phase interfaces). For all of these, it is assumed that the Hall-Petch relationship is valid and the appropriate values for  $k^z$  are taken from Wise (1998).

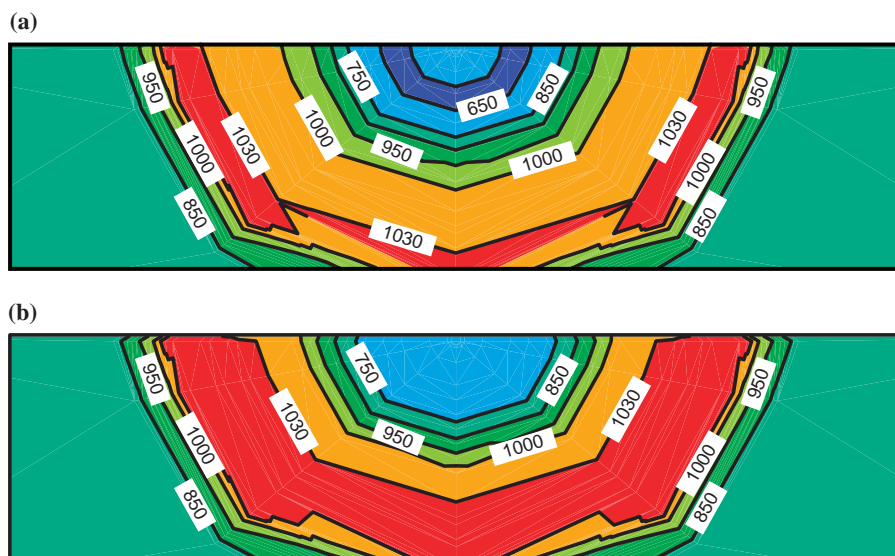
In the previous section, various individual contributions to the material strength have been identified. To combine these contributions, the approach presented by Owen and Grujicic (1986) is used, according to which: the contributions of the mechanisms operating at the same length scale (e.g. solid solution strengthening effects associated with different alloying elements) is governed by the following superposition law:

$$\Delta\tau_{\text{sum}} = \left( \sum_j (\Delta\tau_j)^{1/n} \right)^n \quad (9)$$

where subscripts sum and  $j$  are used to denote, respectively, the outcome of the superposition and the identity of the individual contributions,  $n$  ( $=2.0$ ); and the contributions of the mechanisms operating at different length scales (e.g. solid solution strengthening and precipitate hardening) could be combined using a simple linear-superposition principle. The linear superposition principle is also governed by Equation (9), in which  $n$  is set to 1.0. Details of these two superposition approaches can be found in Owen and Grujicic (1986). When the contribution of all strengthening mechanisms is accounted for through the application of the aforementioned superposition methods, one obtains the total critical resolved shear stress for dislocation glide (i.e. the material shear strength). Using the von Mises yield function, the material shear strength is then converted into the material normal strength by multiplying it with a factor,  $\sqrt{3}$ .

Application of the superposition methods described above results in the prediction of the normal strength at a given material point within the weld. Knowledge of the spatial distribution of material strength within the weld is critical for predicting the overall structural performance (including ballistic-penetration resistance) of the weldment. However, the knowledge of this distribution cannot be directly used to validate the present multi-physics GMAW process model since this would require fabrication and testing of a large number of micron-sized tensile/compression specimens. Typically, it is a distribution of indentation hardness (or, more precisely, micro/nano-hardness) over the transverse (or some other) section of the weldment that is used to characterize the distribution of mechanical properties throughout the weld region. Thus, it is desirable to convert the strength distribution data which are yielded by the improved microstructure/property prediction module into the corresponding hardness distribution. Following Ashby and Jones (1980), material hardness (expressed in the same units as the normal strength) can be calculated by multiplying the normal strength by a factor of 3.0. However, Vickers micro-hardness tests typically quantify material hardness in terms of the so-called Vickers Hardness Number (VHN) which is the material hardness expressed in units of  $\text{kgf/mm}^2$ . To obtain VHN, the material hardness, expressed in MPa, should be divided by a factor of 9.81.

The results presented in this section are counterparts of the results presented in Figure 16(a)-(f). Spatial distribution of the MIL A46100 VHN within the weld region is depicted in Figure 17(a). Examination of the results displayed in this figure reveals that: the material within the FZ which possesses the as-cast microstructure dominated by allotriomorphic and Widmanstatten ferrite has a hardness which is lower than that in the as-received condition of the material,  $\text{VHN} = 750$ ; there is a region (i.e. the previously mentioned "intercritical region") within which the material possesses a hardness substantially higher than the one in the as-received material; and both the low-hardness and the high-hardness regions are of concern since the low-hardness region compromises the load-bearing capacity of the weldment while the high-hardness



**Notes:** (a) Computed in the present work; and (b) as reconstructed using the results reported by Unfried *et al.* (2009)

**Figure 17.**  
Typical spatial  
distribution of the  
material VHN hardness  
within the weld region  
of MIL A46100

region, through the accompanying loss of toughness/ductility, may compromise weldment reliability/durability.

At present, the results displayed in Figure 17(a) could not be validated using in-house welding and testing facilities. GMAW experimental facilities are currently being developed/assembled in order to support our ongoing GMAW modeling and simulation efforts. Once these facilities have been completed, they will enable a full quantitative validation of the present multi-physics GMAW process model. To provide some level of validation for the present model, hardness distribution results reported by Unfried *et al.* (2009) are utilized. However, these results had to be treated with caution in order to account for the effect of some chemical-composition differences between the filler-metal and the workpiece materials. These differences affect the chemical composition, phase/micro-constituent and hardness distributions within the FZ and the adjacent regions of the HAZ (the regions which have experienced changes in their chemical composition due to the solid-state diffusion effects). The reconstructed VHN distribution plot from Unfried *et al.* (2009) is depicted in Figure 17(b). A comparison of the results depicted in Figure 17(a)-(b) reveals that, in the HAZ regions which are located further away from the FZ/HAZ interface and which are not subjected to the solid-state diffusion effects, the agreement between the two sets of results is reasonable.

### 3. Summary and conclusions

- (1) Our recently developed multi-physics five-module computational model for the conventional GMAW joining process has been critically assessed. It was found that the fifth module, the microstructure/property relationship module, needs to be improved in order to be on par with the remaining modules.

- (2) Consequently, improvements are proposed for the microstructure/property relationship module in order to predict the distribution of the material hardness/strength within the weld by assessing the contributions of different attendant strengthening mechanisms.
- (3) The improved multi-physics GMAW process model is then applied to the case of butt-welding of MIL A46100, a prototypical low-alloy, high-hardness armor-grade martensitic steel.
- (4) This application clearly demonstrated the potential of the multi-physics GMAW process model to establish functional relationships between the process parameters, e.g. input welding voltage, electrode-to-workpiece distance, filler-metal feed rate, welding-gun speed, etc. and the resulting spatial distribution of the material microstructure (as represented by the volume fractions of various crystallographic phases and micro-constituents as well as by the prior-austenite grain size) and mechanical properties (primarily hardness) within the fusion and the HAZs of the weld.

## References

- Ashby, M.F. (1969), "On the orowan stress", in Argon, A.S. (Ed.), *Physics of Strength and Plasticity*, M.I.T. Press, Cambridge, MA, pp. 404-412.
- Ashby, M.F. and Jones, D.R.H. (1980), *Engineering Materials: An Introduction to their Properties and Application*, Pergamon Press, New York, NY.
- Bhadeshia, H.K.D.H., Svensson, L.-E. and Gretoft, B. (1985), "A model for the development of microstructure in low-alloy steel (Fe-Mn-Si-C) weld deposits", *Acta Metallurgica*, Vol. 33 No. 7, pp. 1271-1283.
- Dassault Systemes (2011), "ABAQUS Version 6.10EF, User Documentation, Providence, RI.
- Fleischer, R.L. (1963), "Substitutional solution hardening", *Acta Metallurgica et Materialia*, Vol. 11 No. 3, pp. 203-209.
- Gore, M., Grujicic, M. and Olson, G.B. (1989), "Thermally activated grain boundary motion through a dispersion of particles", *Acta Metallurgica*, Vol. 37 No. 7, pp. 2849-2854.
- Grujicic, M. (1989), "Coherent precipitation of  $M_2C$  carbides in AF1410 steel", *Materials Science and Engineering A*, Vol. 117, September, pp. 215-220.
- Grujicic, M., Lai, S.G. and Gumbsch, P. (1997), "Atomistic simulation study of the effect of martensitic transformation volume change on crack-tip material evolution and fracture toughness", *Materials Science and Engineering A*, Vol. 231 Nos 1/2, pp. 151-162.
- Grujicic, M., Ling, H.C., Haezebrouck, D.M. and Owen, W.S. (1992), "The growth of martensite", in Olson, G.B. and Owen, W.S. (Eds), *Martensite*, ASM International, Materials Park, OH, pp. 175-196.
- Grujicic, M., Arakere, G., Pandurangan, B., Hariharan, A., Yen, C.-F., Cheeseman, B.A. and Fountzoulas, C. (2010a), "Computational analysis and experimental validation of the Ti-6Al-4V friction stir welding behavior", *Journal of Engineering Manufacture*, Vol. 225 No. 2, pp. 208-223.
- Grujicic, M., Arakere, G., Yalavarthy, H.V., He, T., Yen, C.-F. and Cheeseman, B.A. (2010c), "Modeling of AA5083 material-microstructure evolution during butt friction-stir welding", *Journal of Materials Engineering and Performance*, Vol. 19 No. 5, pp. 672-684.
- Grujicic, M., He, T., Arakere, G., Yalavarthy, H.V., Yen, C.-F. and Cheeseman, B.A. (2010b), "Fully-coupled thermo-mechanical finite-element investigation of material evolution during friction-stir welding of AA5083", *Journal of Engineering Manufacture*, Vol. 224 No. 4, pp. 609-625.

- Grujicic, M., Arakere, G., Pandurangan, B., Hariharan, A., Yen, C.-F. and Cheeseman, B.A. (2011a), "Development of a robust and cost-effective friction stir welding process for use in advanced military vehicle structures", *Journal of Materials Engineering and Performance*, Vol. 20 No. 1, pp. 11-23.
- Grujicic, M., Arakere, G., Pandurangan, B., Hariharan, A., Yen, C.-F., Cheeseman, B.A. and Fountzoulas, C. (2011b), "Statistical analysis of high-cycle fatigue behavior of friction stir welded AA5083-H321", *Journal of Materials Engineering and Performance*, Vol. 20 No. 6, pp. 855-864.
- Grujicic, M., Arakere, G., Yen, C.-F. and Cheeseman, B.A. (2011c), "Computational investigation of hardness evolution during friction-stir welding of AA5083 and AA2139 aluminum alloys", *Journal of Materials Engineering and Performance*, Vol. 20 No. 7, pp. 1097-1108.
- Grujicic, M., Arakere, G., Hariharan, A. and Pandurangan, B. (2012a), "A concurrent product-development approach for friction-stir welded vehicle-underbody structures", *Journal of Materials Engineering and Performance*, Vol. 21 No. 4, pp. 437-449.
- Grujicic, M., Arakere, G., Hariharan, A. and Pandurangan, B. (2012b), "Two-level weld-material homogenization approach for efficient computational analysis of welded structure blast survivability", *Journal of Materials Engineering and Performance*, Vol. 21 No. 6, pp. 786-796.
- Grujicic, M., Arakere, G., Pandurangan, B., Ochterbeck, J.M., Yen, C.-F., Cheeseman, B.A., Reynolds, A.P. and Sutton, M.A. (2012c), "Computational analysis of material flow during friction stir welding of AA5059 aluminum alloys", *Journal of Materials Engineering and Performance*, Vol. 21 No. 9, pp. 1824-1840.
- Grujicic, M., Pandurangan, B., Yen, C.-F. and Cheeseman, B.A. (2012d), "Modifications in the AA5083 Johnson-cook material model for use in friction stir welding computational analyses", *Journal of Materials Engineering and Performance*, Vol. 21 No. 11, pp. 2207-2217.
- Grujicic, M., Ramaswami, S., Snipes, J.S., Yavari, R., Arakere, A., Yen, C.-F. and Cheeseman, B.A. (2013a), "Computational modeling of microstructure evolution in AISI 1005 steel during gas metal arc butt welding", *Journal of Materials Engineering and Performance*, Vol. 22 No. 5, pp. 1209-1222.
- Grujicic, M., Arakere, A., Ramaswami, S., Snipes, J.S., Yavari, R., Yen, C.-F., Cheeseman, B.A. and Montgomery, J.S. (2013b), "Gas metal arc welding process modeling and prediction of weld microstructure in MIL A46100 armor-grade martensitic steel", *Journal of Materials Engineering and Performance*, Vol. 22 No. 6, pp. 1541-1557.
- Grujicic, M., Ramaswami, S., Snipes, J.S., Yen, C.-F., Cheeseman, B.A. and Montgomery, J.S. (2013c), "Multi-physics modeling and simulations of MIL A46100 armor-grade martensitic steel gas metal arc welding process", *Journal of Materials Engineering and Performance*, *accepted for publication*, Vol. 22 No. 10, pp. 2950-2969.
- Grujicic, M., Galgalikar, R., Snipes, J.S., Yavari, R. and Ramaswami, S. (2013d), "Multi-physics modeling of the fabrication and dynamic performance of all-metal auxetic-hexagonal sandwich-structures", *Materials and Design*, Vol. 51, October, pp. 113-130.
- Johnson, G.R. and Cook, W.H. (1983), "A constitutive model and data for metals subjected to large strains, high strain rates and high temperatures", *Proceedings of the 7th International Symposium on Ballistics, the Hague, American Defense Preparedness Association and Koninklijk Instituut van Ingenieurs*, pp. 541-547.
- Jones, S.J. and Bhadeshia, H.K.D.H. (1997), "Kinetics of the simultaneous decomposition of austenite into several transformation products", *Acta Materialia*, Vol. 45 No. 7, pp. 2911-2920.
- Keh, A.S. and Weissman, S. (1963), "Deformation structure in body-centered cubic metals", in Thomas, G. and Washburn, J. (Eds), *Electron Microscopy and Strength of Crystals*, Interscience, New York, NY, pp. 231-300.
- Kim, D. (2012), "Prediction of microstructure evolution of heat-affected zone in gas metal arc welding of steels", PhD University of Texas, Austin, TX.

- Labusch, R. (1970), "A statistical theory of solid solution hardening", *Physica Status Solidi*, Vol. 41 No. 2, pp. 659-669.
- Leslie, W.C., Michalak, J.T. and Aul, F.W. (1963), "The annealing of cold-worked iron", in Spencer, C.W. and Werner, F.E. (Eds), *Iron and its Dilute Solid Solutions*, Interscience, New York, NY, pp. 119-212.
- Kruger, P. (1993), "On the relation between non-isothermal and isothermal Kolmogorov-Johnson-Mehl-Avrami crystallization kinetics", *Journal of Physics and Chemistry of Solids*, Vol. 54 No. 11, pp. 1549-1555.
- Matsuda, H. and Bhadeshia, H.K.D.H. (2004), "Kinetics of the bainite transformation", *Proceedings of the Royal Society of London A*, Vol. 460 No. 2046, pp. 1707-1722.
- Owen, W.S. and Grujicic, M. (1986), *Plastic Deformation: Thermally Activated Glide of Dislocations*, Encyclopedia of Materials Science and Engineering, Pergamon Press, Oxford, pp. 3540-3543.
- Pavelic, V., Tanbakuchi, R., Uyehara, O.A. and Myers, P.S. (1969), "Experimental and computed temperature histories in gas tungsten-arc welding of thin plates", *Welding Journal Research Supplement*, Vol. 48 No. 7, pp. 295-305.
- Takahashi, M. and Bhadeshia, H.K.D.H. (1990), "Model for transition from upper bainite to lower bainite", *Materials Science and Technology*, Vol. 6 No. 7, pp. 592-603.
- Unfried, S.J., Garzón, C.M. and Giraldo, J.E. (2009), "Numerical and experimental analysis of microstructure evolution during arc welding in armor plate steels", *Journal of Materials Processing Technology*, Vol. 209 No. 4, pp. 1688-1700.
- US Department of Defense (1983), *MIL STD-A46100 Standard Specification: Armor Plate Steel Wrought High Hardness*, Department of Defense, Washington, DC.
- Wells, M.G.H., Weiss, R.K. and Montgomery, J.S. (1992), *LAV Armor Plate Study*, US Army Materials Technology Laboratory, Watertown, MA.
- Wise, J.P. (1998), "Systems design of advanced gear steels", PhD Northwestern University, Evanston, IL.

#### About the authors

M. Grujicic, Clemson University, Professor, Mechanical Engineering. Research interests include computational engineering. Professor M. Grujicic is the corresponding author and can be contacted at: gmica@clemson.edu

Dr J.S.Snipes, Clemson University, Post-Doctoral Fellow, Mechanical Engineering. Research interests include computational material modeling.

R. Galgalikar, Clemson University, Doctoral Student, Mechanical Engineering. Research interests include computer engineering methods and tools.

Dr S. Ramaswami, Clemson University, Post-Doctoral Fellow, Mechanical Engineering. Research interests include computational material modeling.

R. Yavari, Clemson University, Master's Student, Mechanical Engineering. Research interests include multi-physics modeling of various materials phenomena and processes.

Dr C.-F. Yen, Army Research Labs, Aberdeen Proving Ground, Research Engineer, Research interests include composite modeling.

Dr B.A. Cheeseman, Research Labs, Aberdeen Proving Ground, Research Engineer, Research interests include blast modeling and simulation.

Dr J.S. Montgomery, Research Labs, Aberdeen Proving Ground, Research Engineer, Research interests include development of quality standards for materials used on military vehicles.